

IMPROVING THE PERFORMANCE OF MONOCRYSTALLINE SILICON
PERC SOLAR CELLS BY OPTIMIZING FRONT AND REAR
METALLIZATION

A THESIS SUBMITTED TO
THE GRADUATE SCHOOL OF NATURAL AND APPLIED SCIENCES
OF
MIDDLE EAST TECHNICAL UNIVERSITY

BY

HASAN ASAV

IN PARTIAL FULFILLMENT OF THE REQUIREMENTS
FOR
THE DEGREE OF MASTER OF SCIENCE
IN
MICRO AND NANOTECHNOLOGY

JUNE 2022

Approval of the thesis:

**IMPROVING THE PERFORMANCE OF MONOCRYSTALLINE SILICON
PERC SOLAR CELLS BY OPTIMIZING FRONT AND REAR
METALLIZATION**

submitted by **HASAN ASAV** in partial fulfillment of the requirements for the degree
of **Master of Science in Micro and Nanotechnology, Middle East Technical
University** by,

Prof. Dr. Halil Kalıpçılar
Dean, Graduate School of **Natural and Applied Sciences** _____

Prof. Dr. Deniz Üner
Head of the Department, **Micro and Nanotechnology** _____

Prof. Dr. Raşit Turan
Supervisor, **Physics, METU** _____

Assoc. Prof. Dr. Selçuk Yerci
Co-Supervisor, **Electrical-Electronics Engineering, METU** _____

Examining Committee Members:

Prof. Dr. Emrah Ünalın
Metallurgical and Materials Engineering, METU _____

Prof. Dr. Raşit Turan
Physics, METU _____

Assist. Prof. Dr. Ihor Pavlov
Physics, METU _____

Assist. Prof. Dr. Abdullah Üzüm
Electrical-Electronics Engineering, Karadeniz Teknik Uni. _____

Assist. Prof. Dr. Veysel Ünsür
Fundamental Sciences in Engineering, Necmettin Erbakan Uni. _____

Date: 20.06.2022

I hereby declare that all information in this document has been obtained and presented in accordance with academic rules and ethical conduct. I also declare that, as required by these rules and conduct, I have fully cited and referenced all material and results that are not original to this work.

Name Last name : HASAN ASAV

Signature :

ABSTRACT

IMPROVING THE PERFORMANCE OF MONOCRYSTALLINE SILICON PERC SOLAR CELLS BY OPTIMIZING FRONT AND REAR METALLIZATION

Asav, Hasan
Master of Science, Micro and Nanotechnology
Supervisor: Prof. Dr. Raşit Turan
Co-Supervisor: Assoc. Prof. Dr. Selçuk Yerci

June 2022, 85 pages

Silicon photovoltaics dominates the solar cell market, accounting for over 95% of the total share. The fabrication process of silicon solar cells includes some crucial steps that have a significant impact on solar cell conversion efficiency. These steps are mainly categorized as surface texturization, diffusion, antireflective coatings, and metallization. Among these crucial steps, metallization is a key step for the reduction and control of the electrical and optical losses of the solar cell. The formation of the electrical contacts is achieved by the metal layers on the front and back surfaces of the solar cell. In this M.Sc. thesis, optimization of the metallization is studied for passivated emitter and rear contact (PERC) solar cells to improve cell performance.

Rear side metal contact formation for the PERC solar cell is strongly linked with the laser contact opening (LCO) process which provides a path from the rear surface of the cell to the silicon substrate. Therefore, optimization of LCO is a necessary part of the study to minimize the losses from the rear passivation stack. With this aim, different LCOs are studied and the optimum metal fraction for the rear side is

performed on the fabricated PERC solar cells. An average of 6 mV cell V_{oc} increase is gained thanks to these optimizations on the rear side.

The metallization process in this study is based on a screen-printing method for the formation of front and rear metal contacts of the PERC solar cell. A GriddlerPro simulation program is utilized to design and simulate the front metal design. Then, the analysis of front metal contacts is done thoroughly.

After these optimizations, the fast-firing step is studied and a newly developed recipe is brought to the ODTÜ-GÜNAM laboratories.

While new cell designs are rapidly growing, our future goals will include following these new advances closely and employing new metallization schemes that can enhance cell performance.

Keywords: PERC solar cell, laser contact opening, metallization, screen-printing, fast-firing

ÖZ

ÖN VE ARKA METALİZASYON OPTİMİZASYONUyla TEK KRİSTAL SİLİSYUM PERC GÜNEŞ HÜCRELERİNİN PERFORMANSINI ARTIRMAK

Asav, Hasan
Yüksek Lisans, Mikro ve Nanoteknoloji
Tez Yöneticisi: Prof. Dr. Raşit Turan
Ortak Tez Yöneticisi: Doç. Dr. Selçuk Yerci

Haziran 2022, 85 Sayfa

Silisyum fotovoltaikler, toplam payın %95'inden fazlasını oluşturan güneş pili pazarına hakimdir. Silisyum güneş pillerinin üretim süreci, güneş pili dönüşüm verimliliği üzerinde önemli bir etkisi olan bazı önemli adımları içerir. Bu adımlar temel olarak yüzey tekstüre etme, difüzyon, yansıma önleyici kaplamalar ve metalizasyon olarak kategorize edilir. Bu önemli adımlar arasında metalizasyon, güneş pilinin elektriksel ve optik kayıplarının azaltılması ve kontrolü için önemli bir adımdır. Elektrik kontaklarının oluşumu, güneş pilinin ön ve arka yüzeylerindeki metal tabakalar ile sağlanır. Bu tez çalışmasında, hücre performansını iyileştirmek için pasifleştirilmiş emitör ve arka temaslı (PERC) güneş pilleri için metalizasyonun optimizasyonu incelenmiştir.

PERC güneş pili için arka taraf metal temas oluşumu, hücrenin arka yüzeyinden silisyum alt tabakaya bir yol sağlayan lazer temas açma (LCO) işlemi ile güçlü bir şekilde bağlantılıdır. Bu nedenle, LCO'nun optimizasyonu, arka pasivasyon yığınının kaynaklanan kayıpları en aza indirmek için çalışmanın gerekli bir parçasıdır. Bu amaçla, farklı LCO'lar çalışılmış ve üretilen PERC güneş pillerinde

arka taraf için optimum metal fraksiyonu gerçekleştirilmiştir. Arka taraftaki bu optimizasyonlar sayesinde ortalama 6 mV hücre V_{oc} artışı elde edilir.

Bu çalışmadaki metalizasyon işlemi, PERC güneş pilinin ön ve arka metal kontaklarının oluşumu için bir serigrafi yöntemine dayanmaktadır. Ön metal tasarımı tasarlamak ve simüle etmek için GriddlerPro simülasyon programı kullanılır. Daha sonra ön metal kontakların analizi detaylı bir şekilde yapılır.

Bu optimizasyonlardan sonra kontak yakma adımı incelenir ve yeni geliştirilen reçete ODTÜ-GÜNAM laboratuvarlarına kazandırılır.

Yeni hücre tasarımları hızla büyürken, gelecekteki hedeflerimiz bu yeni gelişmeleri yakından takip etmeyi ve hücre performansını artıracak yeni metalizasyon şemalarını kullanmayı içerecektir.

Anahtar Kelimeler: PERC güneş hücresi, lazer oyuk açma, metalizasyon, serigrafi, hızlı yakma

To my family...

ACKNOWLEDGMENTS

I would like to thank my supervisor Prof. Dr. Raşit Turan for his great mentorship and for guiding me as a member of ODTÜ-GÜNAM. Each time, I felt his support during my academic research. Also, his support was endless whenever we are in trouble. It was the best decision to make research in his lab under the supervision of Prof. Raşit Turan. I also would like to thank my co-supervisor Assoc. Prof. Dr. Selçuk Yerci for guiding me in my academic career.

I also would like to thank my examining committee members; Prof. Dr. Hüsni Emrah Ünalın, Assist. Dr. Ihor Pavlov, Assist. Dr. Abdullah Üzüm and Assist. Dr. Veysel Ünsür.

I would like to thank Dr. Bülent Arıkan for his guidance and support during my research.

I would like to thank Dr. Gence Bektaş for his endless support and creative-minded solutions to my problems. Also, he left the GPVL metallization line to me in a proper working condition. His efforts cannot be disregarded about the metallization line. Whenever we need help, he did much more.

The special acknowledgment also belongs to Murat Aynacıođlu. He attends each laser and metallization process with me and operates all processes in the best manner.

For texturing and cleaning processes Sümeyye Koçak Bütüner, for diffusion and AlO_x processes, Ahmet Emin Keçeci, for PECVD processes Hasan Hüseyin Canar, for I-V measurements Furkan Çiçek and Batuhan Taş helped me many times. We are a great team with their support. I also would like to thank all ODTÜ-GÜNAM members for being an important ring of the chain.

I also would like to thank my family. They didn't hold back their support in every minute of my life. Also, the deepest thanks belong to my fiancé, Burcu Aksoy. She always supports me in my academic career with her motivated talks.

TABLE OF CONTENTS

ABSTRACT	v
ÖZ.....	vii
ACKNOWLEDGMENTS.....	x
TABLE OF CONTENTS	xii
LIST OF TABLES	xv
LIST OF FIGURES	xvi
LIST OF ABBREVIATIONS	xix
CHAPTERS	
1 INTRODUCTION.....	1
1.1 Global Energy Demand	1
1.1.1 Photovoltaic Technology.....	3
1.2 Types of PV Technology	5
1.3 Summary of the Thesis	6
2 LASER CONTACT OPENING (LCO) AND METALLIZATION PROCESSES FOR PERC SOLAR CELLS	9
2.1 Solar Cell Basics.....	9
2.1.1 Solar Cell Parameters	10
2.2 Production Steps of PERC Solar Cells	12
2.3 Laser Contact Opening (LCO) for PERC Solar Cells	16
2.3.1 BSF and Voided Contact Formation Mechanism.....	16
2.3.2 Laser Parameters	18

2.4	Metallization Techniques for c-Si Solar Cells	22
2.4.1	Screen-Printing	23
2.4.2	Electroplating	24
2.4.3	Evaporation	24
2.4.4	Inkjet Printing	25
2.4.5	Metallization of PERC Solar Cells by Screen-Printing Method.....	25
2.4.6	Metallization Screens	26
2.4.7	Solar Cell Pastes	27
2.4.8	Screen-Printing Methods and Parameters	28
2.4.9	Aspect Ratio	31
2.5	Resistive Losses	32
2.5.1	Series Resistance (R_s)	32
2.5.2	Shunt Resistance (R_{sh})	34
2.5.3	Contact Resistance (R_c).....	35
2.6	Optimization of Front Grid Design	36
3	EXPERIMENTAL DESIGN AND PROCEDURES.....	39
3.1	Production Tools and Experimental Design.....	39
3.1.1	Innolas Laser System	39
3.1.2	Baccini Screen-Printer	42
3.1.3	BTU Fast-Firing Furnace	44
3.1.4	Experimental Procedure and Details for the Fast-Firing Recipe Development	44
3.2	Characterization Tools	48
3.2.1	Solar Cell Tester and Sorter	48
3.2.2	Transmission Line Measurement (TLM).....	49

3.2.3	Line Resistance Measurement	50
3.2.4	Scanning Electron Microscopy (SEM).....	51
3.2.5	Electroluminescence (EL) and Photoluminescence (PL) Imaging....	51
3.2.6	Dark Current-Voltage (I-V) Measurement.....	52
4	EXPERIMENTAL RESULTS	53
4.1	Optimization and Characterization of Rear Metal Contacts.....	53
4.1.1	The Effects of Rear Metal Fraction on Passivation Quality.....	53
4.1.2	The Effects of the LCO Pitch on Solar Cell Performance.....	55
4.1.3	The Effects of LCO Pitch on Contact Characteristics.....	59
4.2	Optimization and Characterization of the Front Metal Contacts	61
4.2.1	Simulation of the Front Metal Grid Design via GriddlerPro.....	61
4.2.2	Process Integration of the Simulated Results	65
4.2.3	The Effects of Fast-Firing Profiles on Contact Characteristics and PV Parameters	67
5	CONCLUSIONS	79
	REFERENCES	81

LIST OF TABLES

TABLES

Table 4.1. <i>Dimensional specifications of the four patterns</i>	54
Table 4.2. <i>Average photovoltaic parameters for each LCO pattern</i>	58
Table 4.3. <i>Statistical contact characteristics of the investigated contacts</i>	60
Table 4.4. <i>Simulation parameters</i>	62
Table 4.5. <i>Final screen specs from simulated data</i>	65
Table 4.6. <i>Specs of the metallization screen</i>	65
Table 4.7. <i>Printing parameters for the snap-off test</i>	66
Table 4.8. <i>Analysis of the regions on three different fast-firing recipes</i>	68
Table 4.9. <i>Fast-firing set temperatures</i>	68
Table 4.10. <i>Analysis of the fast-firing final profile</i>	70
Table 4.11. <i>R_s values of the PERC solar cells produced with two different Ag pastes</i>	72
Table 4.12. <i>PV parameters of the best solar cell fabricated in ODTÜ-GÜNAM</i> ...	76
Table 4.13. <i>R_s of the solar cell fabricated in ODTÜ-GÜNAM</i>	76

LIST OF FIGURES

FIGURES

<i>Figure 1.1.</i> The annual addition of power capacity (GW) by renewables between 2014-2020 [3]	2
<i>Figure 1.2.</i> Share of electricity production from solar energy all over the world [4]	3
<i>Figure 1.3.</i> Cross-section of a commercial monocrystalline silicon solar cell [6]....	4
<i>Figure 1.4.</i> Solar PV market, Global installed capacity, 2016-2025 [8].....	5
<i>Figure 2.1.</i> Dark and illuminated I-V curves with their characteristic points [14].	10
<i>Figure 2.2.</i> Production steps of PERC solar cell.....	12
<i>Figure 2.3.</i> SEM image of the alkaline textured pyramidal surface	13
<i>Figure 2.4.</i> Representation of p-n junction	14
<i>Figure 2.5.</i> SEM image of rear local contact of PERC solar cell	17
<i>Figure 2.6.</i> Voided contact formation	18
<i>Figure 2.7.</i> Absorption coefficient and wavelength relation of silicon.....	20
<i>Figure 2.8.</i> Absorption depth and wavelength relation of silicon.....	20
<i>Figure 2.9.</i> Pulsed laser emission representation [24]	21
<i>Figure 2.10.</i> Schematic representation of screen-printing process [27].....	23
<i>Figure 2.11.</i> Schemical representation of Cu plating.....	24
<i>Figure 2.12.</i> Screen opening channel [31]	26
<i>Figure 2.13.</i> CAD drawing of busbar screen	29
<i>Figure 2.14.</i> CAD drawing of fingers screen.....	30
<i>Figure 2.15.</i> Cross-section view of a finger.....	31
<i>Figure 2.16.</i> An I-V curve of a solar cell [34].....	32
<i>Figure 2.17.</i> Resistances that constitute the R_s [35].....	33
<i>Figure 2.18.</i> Effect of high series resistance on the solar cell I-V curve	33
<i>Figure 2.19.</i> Effect of low shunt resistance on the solar cell I-V curve.....	35
<i>Figure 2.20.</i> Griddler input screen for wafer shape and size	37
<i>Figure 2.21.</i> Griddler input screen for front and rear metallization parameters	37
<i>Figure 2.22.</i> An example of a Griddler simulation result	38
<i>Figure 3.1.</i> InnoLas laser system	40

<i>Figure 3.2.</i> Straight line and dashed line patterns for rear LCO [42]	41
<i>Figure 3.3.</i> Baccini metallization line at ODTÜ-GÜNAM	42
<i>Figure 3.4.</i> The plan for the screen design experiment	43
<i>Figure 3.5.</i> BTU fast-firing furnace in ODTÜ-GÜNAM laboratories	44
<i>Figure 3.6.</i> Fast-firing profile of Heraeus PV	45
<i>Figure 3.7.</i> Fast-firing profile of Fraunhofer ISE	46
<i>Figure 3.8.</i> Standard fast-firing profile of ODTÜ-GÜNAM.....	46
<i>Figure 3.9.</i> Design of the experiment for fast-firing recipe development	48
<i>Figure 3.10.</i> Solar cell tester and sorter in ODTÜ-GÜNAM laboratories	48
<i>Figure 3.11.</i> Reference solar cell I-V result taken from solar cell tester and sorter	49
<i>Figure 3.12.</i> Top and side view of the schematic representation of TLM structure [44].....	49
<i>Figure 3.13.</i> Resistance vs. length graph [44]	50
<i>Figure 3.14.</i> Components of SEM [45]	51
<i>Figure 4.1.</i> iV_{oc} values of the blue wafers lasered by different fractions	54
<i>Figure 4.2.</i> Average iV_{oc} chart of the blue wafers lasered with different contact itches	56
<i>Figure 4.3.</i> PL images for dashed patterns with 900 μm , 1000 μm , 1100 μm , and 1200 μm contact pitches and the line pattern, respectively	57
<i>Figure 4.4.</i> Cell conversion efficiencies of all dashed lines with the reference LCO pattern (line pattern).....	59
<i>Figure 4.5.</i> Well-formed BSF under the LCO with Dash-1000 pattern	61
<i>Figure 4.6.</i> Simulated results of the PERC solar cells with varying front metal fractions.....	63
<i>Figure 4.7.</i> Simulated results of the PERC solar cells with varying finger widths around 5.5% metal fraction.....	64
<i>Figure 4.8.</i> Snap-off distance vs. aspect ratio for Heraeus PV (top) and Pharos Materials (bottom) Ag paste	66
<i>Figure 4.9.</i> Aspect ratios of the Heraeus PV paste [49]	67
<i>Figure 4.10.</i> Initial profile of ODTÜ-GÜNAM.....	71

<i>Figure 4.11.</i> Final profile of ODTÜ-GÜNAM	71
<i>Figure 4.12.</i> Comparison of the cell results printed with Heraeus and Pharos pastes	72
<i>Figure 4.13.</i> Contact resistivities of the metal fingers printed with Heraeus PV Ag paste	73
<i>Figure 4.14.</i> Contact resistivities of the metal fingers printed with Pharos Mat. Ag paste	74
<i>Figure 4.15.</i> SEM image of the metal finger printed with Heraeus PV Ag paste...	75
<i>Figure 4.16.</i> SEM image of the metal finger printed with Pharos Materials Ag paste	75
<i>Figure 4.17.</i> Contact resistivity mapping of the ODTÜ-GÜNAM cells.....	77

LIST OF ABBREVIATIONS

ABBREVIATIONS

4PP	Four-point probe
AM	Air Mass
Ag	Silver
AlO _x	Aluminum Oxide
Al	Aluminum
Al-Si	Aluminum-Silicon
B	Boron
BSF	Back Surface Field
CAD	Computer Aided Drawing
CNC	Computer Numerical Control
CO ₂	Carbon dioxide
c-Si	Crystalline silicon
Cu	Copper
Cz	Czochralski
D	Diameter
D ₀	Wire to wire distance
d	Wire diameter
ECV	Electrochemical Capacitance-Voltage
EL	Electroluminescence

EOM	Emulsion Over Mesh
FF	Fill factor
f	Frequency
H ₃ BO ₄	Boric acid
I _{SC}	Short-circuit current
I _L	Light-generated current
I ₀	Dark-saturation current
I _{MP}	Maximum current point
J _{SC}	Short-circuit current density
k	Boltzmann constant
KOH	Potassium hydroxide
kHz	Kilohertz
MC	Mesh-count
MHz	Megahertz
mV	Millivolt
Nickel	Ni
N	Newton
n	Ideality factor
nm	Nanometer
NaOH	Sodium hydroxide
OA	Opening Area
P	Phosphorus

P_{IN}	Input power
P_{MP}	Maximum power point
P_{max}	Maximum power
PECVD	Plasma-Enhanced Chemical Vapor Deposition
PERC	Passivated Emitter and Rear Cell
PCE	Power Conversion Efficiency
PL	Photoluminescence
PLC	Programmable Logic Controller
ps	Picosecond
PV	Photovoltaic
R_{CH}	Characteristic resistance
R_C	Contact resistance
R_S	Series resistance
R_{SH}	Shunt resistance
R_{Sheet}	Sheet resistance
SEM	Scanning Electron Microscopy
SiN_x	Silicon Nitride
SRV	Surface Recombination Velocity
T	Temperature
TLM	Transmission Electron Microscopy
V	Voltage
V_{OC}	Open-circuit voltage

W_n	Screen opening
QSSPC	Quasi-steady-state photoconductance
ρ_c	Specific contact resistivity
q	Elementary charge
Φ	Angle

CHAPTER 1

INTRODUCTION

1.1 Global Energy Demand

Energy use is by far the main source of greenhouse gas emissions from human activities on a global scale. Burning fossil fuels to supply energy for heating, power, transportation, and industry accounts for almost two-thirds of worldwide greenhouse gas emissions [1]. The possible consequences of continuing to use fossil fuels to meet ever-increasing energy demands linked with population growth and per capita energy consumption could be disastrous for the environment and lead to the exhaustion of the world's limited fossil fuel sources. Both developed and developing countries face this difficulty. As a result, a major transformation of our energy infrastructure to one that is cleaner, renewable, efficient, carbon-free, and environmentally friendly is critically needed.

Our energy consumption and production have a significant impact on the climate. Climate change can modify our energy generation capacity as well as our energy requirements. For instance, changes in the water cycle with less rainfall may lead to warmer temperatures. Therefore, it increases the energy demand for cooling in the summer while lowering the demand for heating in the winter.

Since there is an increasing energy demand globally, the utilization of renewable sources has a profound impact on fulfilling the needs all over the world. Renewables are expected to account for about 30% of electricity output in 2021, up from less than 27% in 2019 [2]. In this sense, while renewables are becoming widespread; increasing their reliability, expanding transmission, and improving grid integration should be the major goals as well as keeping them affordable.

Figure 1.1 illustrates the addition of power capacity by renewable sources between the years 2014 and 2020. In 2020, solar photovoltaics (PV) has a huge contribution to the addition of power capacity among other renewables.

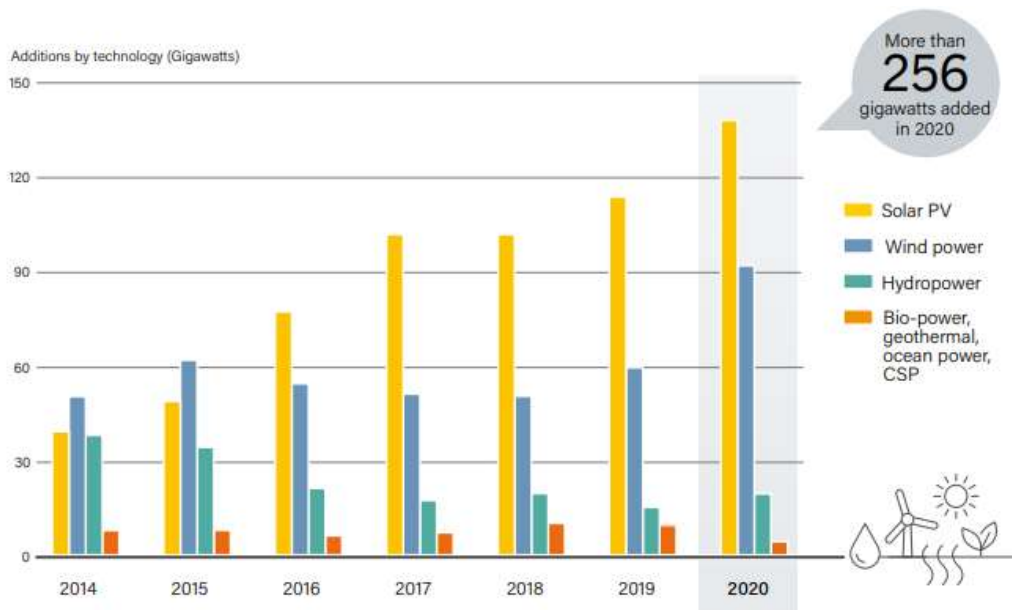


Figure 1.1. The annual addition of power capacity (GW) by renewables between 2014-2020 [3]

Photovoltaics is emerging as a strong alternative energy technology that can mitigate the problems related to climate change. Sun generates limitless energy. If it can be harnessed efficiently, an ideal solution is found to the growing need for clean energy sources. Solar energy has several advantages, including the fact that it is non-polluting, clean, and available all year.

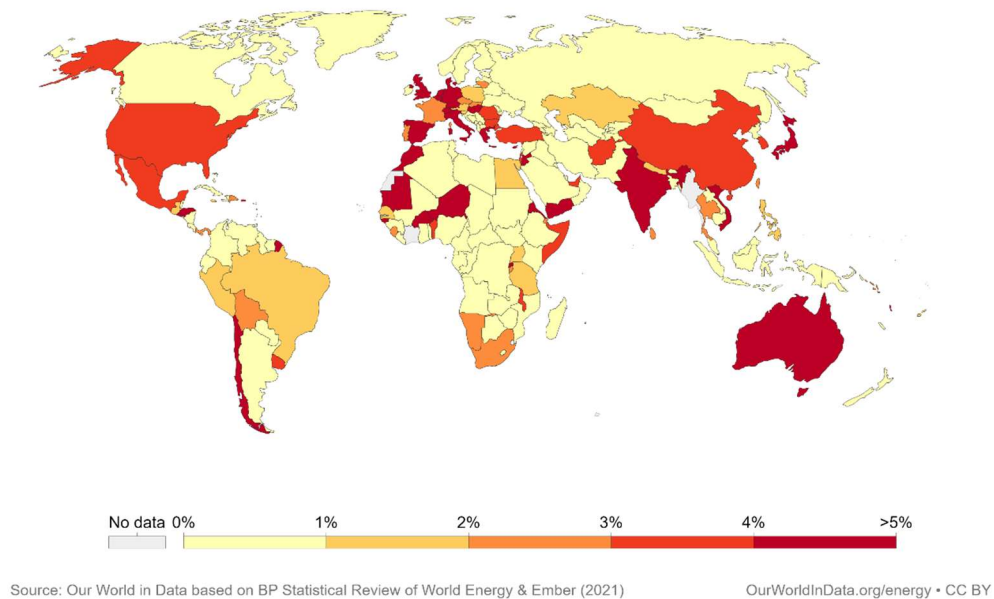


Figure 1.2. Share of electricity production from solar energy all over the world [4]

The total share of electricity production all over the world is still steadily increasing as depicted in Figure 1.2. While solar energy is becoming widespread thanks to its several advantages mentioned before, it is also being affordable throughout the years [5].

1.1.1 Photovoltaic Technology

Silicon (Si) is the second most abundant element in Earth's crust. It is a dominant material used in photovoltaic technology. The most popular solar cells on the market are crystalline silicon PV cells, which have the best performance in terms of conversion efficiency and cost. Silicon PV cells have a significant track record of successful field operations. Figure 1.3 shows the structure of typical commercial crystalline silicon solar cells [6].

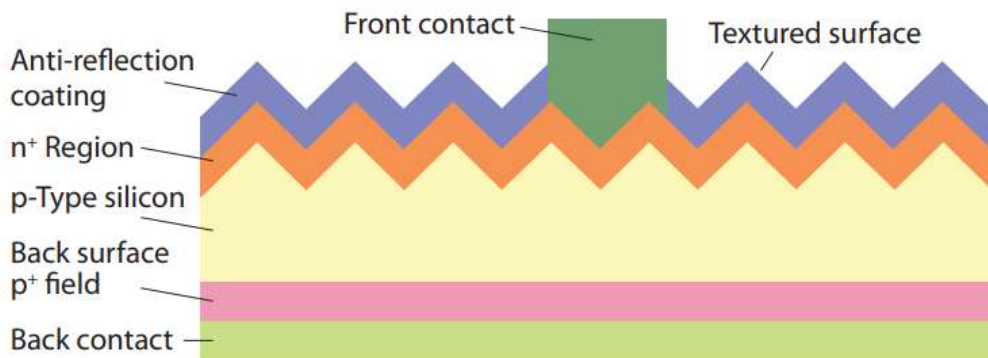


Figure 1.3. Cross-section of a commercial monocrystalline silicon solar cell [6]

The main advantage of silicon PV cells is that solar energy can be directly converted to electrical energy. There are some other advantages of silicon PV cells as follows [7]:

- 1) Si solar cell is proven to be reliable and robust
- 2) A conventional industrial silicon PV cell has higher efficiency/cost performance than any other single-junction device on the market. We need fewer solar cells to obtain the same power output.
- 3) Crystalline silicon cells have a 25-year module lifetime and show little long-term degradation.
- 4) It is an environmentally friendly technology. There is no CO₂ emission during the operation. Since silicon is not a poisonous element, this technology does not threaten the living environment.

These advantages bring about the popularity of silicon PV cells among other renewable energy sources. Therefore, installed solar PV capacity is steadily increasing each year. Figure 1.4 shows the global total solar PV market scenarios from 2016 to 2025.

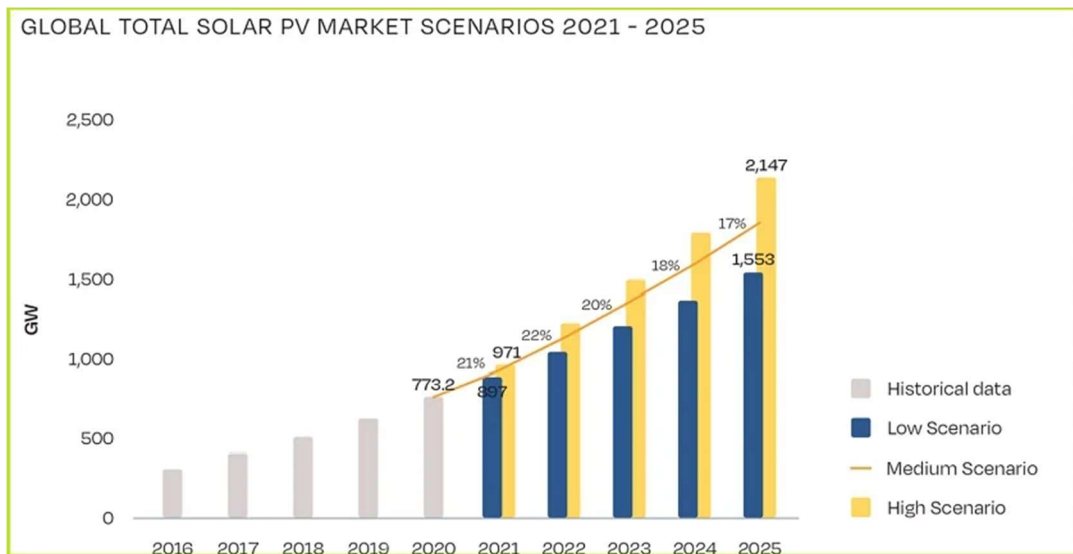


Figure 1.4. Solar PV market, Global installed capacity, 2016-2025 [8]

1.2 Types of PV Technology

PV technology includes various types which have been developed through the years. Some of these technologies have reached a good maturity level and commercial success, some have not.

Solar cells manufactured from monocrystalline silicon are indeed the oldest ones among the others. They're built of pure silicon crystal, which has an ordered lattice and few imperfections. They are also preferred because of their robustness and they are durable for up to 25 years. [11]

Polycrystalline cells have multiple grains of silicon crystals into thin wafers. Monocrystalline silicon is obtained by the polycrystalline form of silicon after some processes. Therefore, polycrystalline silicon is cheaper than monocrystalline silicon. However, solar cells made up of polycrystalline silicon are less efficient than solar cells produced from monocrystalline silicon.

Another type of PV technology is thin-film PV cells which are produced from silicon film deposited on the glass substrate [11]. The main advantage of this technology is that it has less silicon usage compared to monocrystalline and polycrystalline cells.

Therefore, it is cheaper than the c-Si technology. However, the power conversion efficiency of amorphous silicon thin-film solar cells is much less than c-Si PV cells. Their contribution to the PV market share is suppressed for this reason.

Cadmium Telluride (CdTe) PV is another type of thin-film PV technology. Because of the cheaper cost per kW-hour [11], it has become extremely popular. CdTe cells have the advantage of being able to catch shorter wavelengths of light than silicon cells. There are some environmental worries about tellurium's limited supply and possibly harmful effects.

Copper Indium Gallium Selenide (CIGS) PV has become a popular new material for solar cells since it does not contain hazardous Cd and has greater efficiency. While laboratory studies showed that this type of photovoltaics has a lot of potentials, mass production of CIGS has proven to be a challenge. Thin-film deposition on a substrate, which can also be flexible, is used to make CIGS cells (unlike silicon cells). The CIGS cells, like CdTe cells, have a high resistance to heating.

Furthermore, the emerging type of PV technology, polymer, and organic PV technology, enables cells to be small and light compared to silicon cells. They also provide flexibility and a low cost of fabrication. They are, however, far less efficient such as approximately 1/3 of the efficiency of a normal Si cell, and sometimes more prone to deterioration.

1.3 Summary of the Thesis

This work is based on the passivated emitter and rear contact (PERC) solar cell front and rear side metallization processes. In Chapter 2, the main focus is on the description of the PERC solar cell production steps, especially on the laser contact opening (LCO) and metallization. The mechanism behind these processes is discussed thoroughly. Different techniques which can be used for the metallization of PERC solar cells, and metallization screen optimization by using the Griddler Pro simulation program are also the content of Chapter 2. In Chapter 3, the experimental

setup and characterization methods used throughout the study will be discussed. In Chapter 4, experimental results and optimizations about PERC cell LCO and metallization processes that are conducted in the ODTÜ-GÜNAM pilot production line will be shared. In Chapter 5, the results from the experiments that we conducted, and our future goals will be shared.

CHAPTER 2

LASER CONTACT OPENING (LCO) AND METALLIZATION PROCESSES FOR PERC SOLAR CELLS

This chapter provides a detailed presentation of the metallization processes in c-Si solar cells, especially for PERC solar cells. First, the solar cell basics including PV parameters are discussed. Then, metallization techniques for front and rear surfaces are the other focus of this chapter. At the end of this chapter, resistive losses in the solar cell are shown, and an optimization program “Griddler” which was used during our study is introduced.

2.1 Solar Cell Basics

A typical silicon solar cell is made up of a thin wafer with a phosphorus-doped (n-type) silicon layer formed in the surface region of a boron-doped (p-type) silicon wafer[12]. The p-n junction formed in this way creates an electrical field that provides the main mechanisms to separate the electron-hole pairs formed upon optical absorption.

When sunlight strikes the surface of a PV cell, light-stimulated electrons gain momentum resulting in a current flow [12]. The equation for the I-V curve is represented by the Equation 2.1

$$I = I_0 \left[\exp \left(\frac{qV}{nkT} \right) - 1 \right] - I_L \quad \text{Eq.(2.1)}$$

The superposition of the I-V curve of the solar cell diode in the dark with the light-generated current gives the IV curve of a solar cell as shown in Figure 2.1 [13].

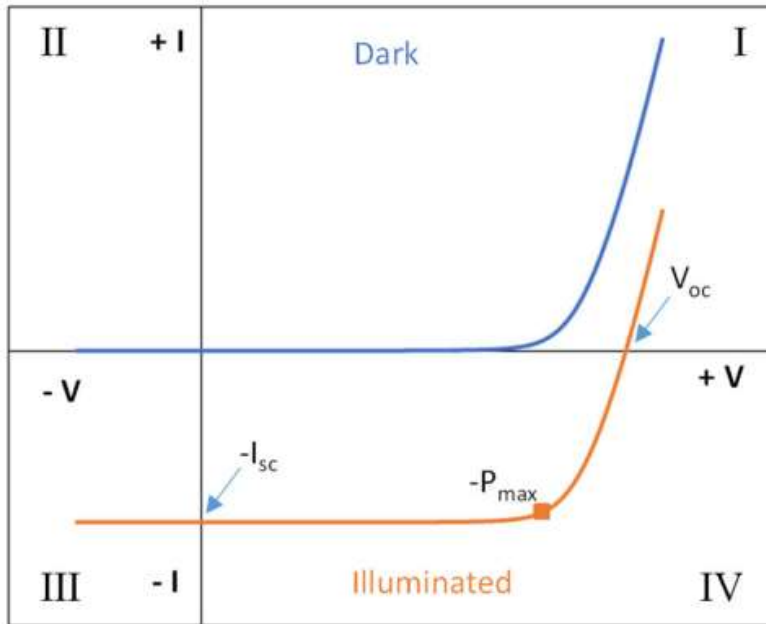


Figure 2.1. Dark and illuminated I-V curves with their characteristic points [14]

2.1.1 Solar Cell Parameters

2.1.1.1 Open-Circuit Voltage (V_{oc})

The open-circuit voltage is referred to as the maximum voltage that can be extracted from a solar cell when the net current through the device is zero. The forward bias on the solar cell due to the bias of the solar cell junction with the light-generated current is represented by the open-circuit voltage. The open-circuit voltage of a solar cell is represented in Equation 2.2.

$$V_{oc} = \frac{nkT}{q} \cdot \ln\left(\left(\frac{I_L}{I_0}\right) + 1\right) \quad \text{Eq. (2.2)}$$

where n , k , T , q , I_L , and I_0 represent ideality factor, Boltzmann constant, temperature, charge, light generated current, and dark saturation current, respectively.

2.1.1.2 Fill Factor (FF)

The power of the solar cell is determined by the product of the open-circuit voltage and the current at the maximum power point (I_{MP}). Fill factor is defined as the ratio of maximum power point (P_{MP}) to the product of open-circuit voltage and short-circuit current (I_{SC}) which will be described in the next section.

$$FF = \frac{P_{MP}}{V_{OC} I_{SC}} \quad \text{Eq. (2.3)}$$

The FF is a measure of the squareness of the I-V curve.

2.1.1.3 Short-Circuit Current (I_{sc})

When the solar cell is short-circuited, the obtained current is named a short circuit current [15]. This parameter depends on the area of the solar cell. Therefore, it is converted to the short circuit current density (J_{SC}) to get rid of the area dependence. Also, the power of the incident source has a significant effect on the I_{sc} . The spectrum of the incident light, optical properties of the solar cell, and the collection probability of the solar cell are the other environmental effects on the short circuit current.

2.1.1.4 Power Conversion Efficiency (PCE)

Power conversion efficiency defines how much percent of luminous power (input power, P_{IN}) falling on the solar cell is converted to the photovoltaically generated electric output of the cell [15]. The spectrum and intensity of the incident sunlight influence the PCE measurements. Therefore, terrestrial solar cells should be measured under AM 1.5 conditions and at a temperature of 25 °C.

The maximum power and PCE calculation of a solar cell are denoted in Equation 2.4 and Equation 2.5.

$$P_{MAX} = V_{OC} I_{SC} FF \quad \text{Eq. (2.4)}$$

$$\eta = \frac{V_{OC} I_{SC} FF}{P_{IN}} \quad \text{Eq. (2.5)}$$

During the study, the PCE of the produced solar cells is measured by using calibrated (AM 1.5G) solar simulator.

2.2 Production Steps of PERC Solar Cells

This section provides information about the production steps of monocrystalline silicon PERC solar cells.

Figure 2.2 shows the all production steps for the fabrication of PERC solar cells.

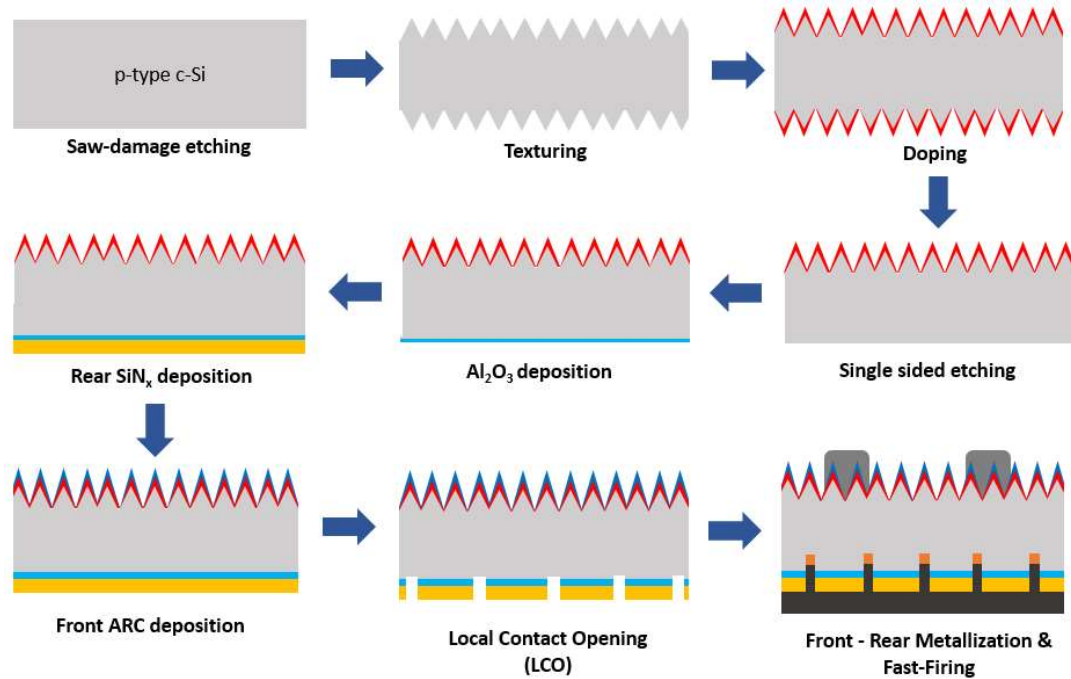


Figure 2.2. Production steps of PERC solar cell

Saw-Damage Etching: Crystalline silicon growth can be achieved by either Czochralski or float-zone techniques. There are some mechanical processes to obtain a wafer. During these mechanical processes, the surface of the wafer is damaged and there is needed a chemical treatment so-called saw-damage etching. Sodium hydroxide (NaOH) and potassium hydroxide (KOH) are the generally used chemicals to etch the surface of the wafers by 5-10 μm [16].

Alkaline Texturing: Monocrystalline silicon wafers with [100] orientation are the most common type among all monocrystalline silicon wafers since etching of the surface of [100] orientation can be achieved easily by using alkaline etchant like KOH. Since the etching of [100] surface is anisotropic by KOH, this process creates pyramids on the surface of the wafer. The reason behind the formation of these pyramids is that alkaline etchants etch [100] silicon surface faster than [111] silicon surface [17]. Figure 2.3 is a scanning electron microscopy (SEM) image of the textured wafer in ODTÜ-GÜNAM laboratories.

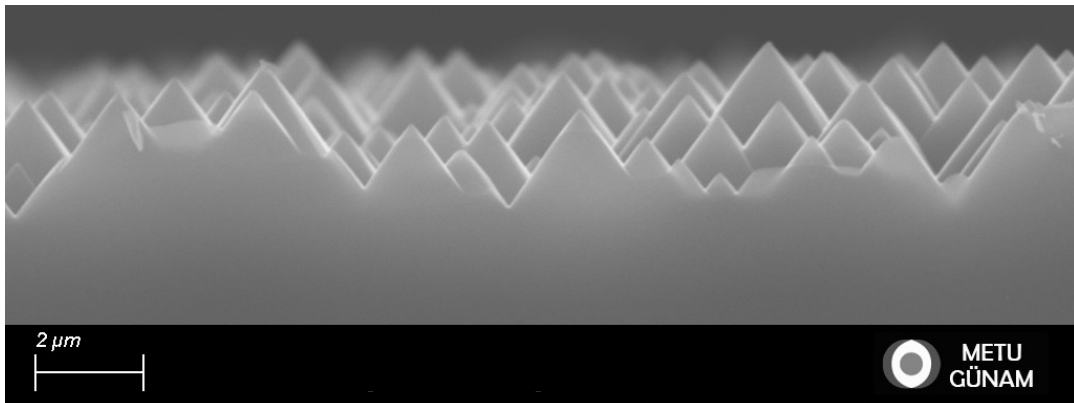


Figure 2.3. SEM image of the alkaline textured pyramidal surface

Doping: Diffusion is a key process introducing a controlled amount of elements into semiconductors and altering the conductivity type. These elements, either boron (B) or phosphorus (P), are introduced commonly in liquid or gaseous form at high temperatures to make a contact with the silicon wafer. This diffusion process creates an emitter depending on the precursor which contains B or P. Production of PERC

solar cells requires a p-type silicon substrate and doping with phosphorus makes the surface n-type since P is a group (V) element. The formed junction creates an electric field that separates the generated electron-hole pairs from each other. As a result, photogenerated carriers are formed.

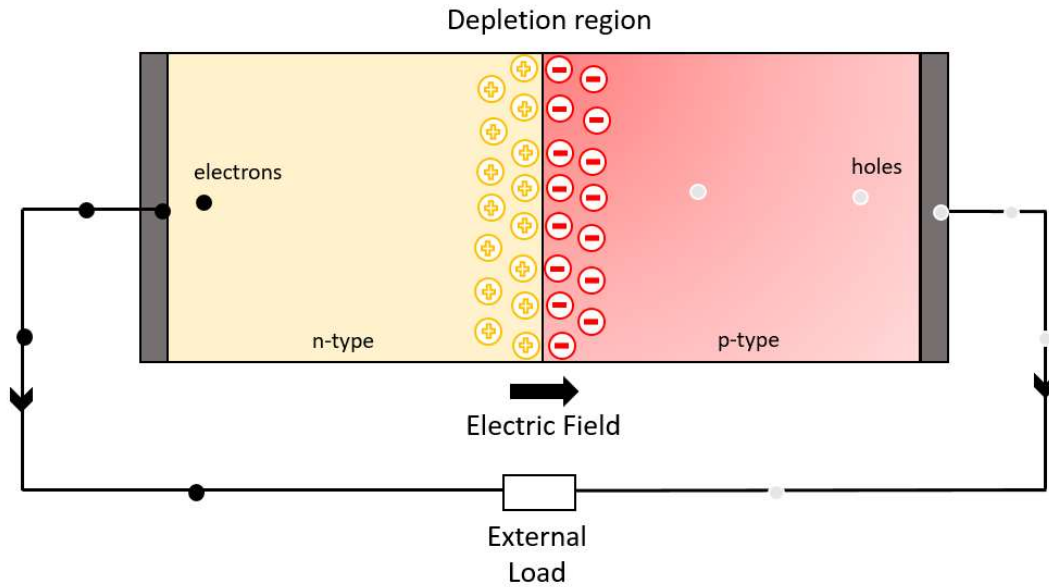


Figure 2.4. Representation of p-n junction

Single-Sided Etching (SSE): Rear side of the wafer is etched with chemical solutions to increase the reflection ability from the rear surface of the solar cell. When the sunlight hits the front surface of the solar cell, some wavelengths (especially infrared) of the light can reach the rear surface. To convert this light into electricity, the increased reflection of the rear side provides an additional current gain to the electrical load. The SSE process is achieved by the industrial RENA InPilot tool which can process 4000 wafers/hour in ODTÜ-GÜNAM laboratories.

AlO_x Deposition: Rear side passivation stack layer is composed of thin aluminum oxide (AlO_x) and silicon nitrate (SiN_x) layers. The AlO_x layer with an appropriate thickness can be deposited by Atomic Layer Deposition (ALD) tool. Deposition of the AlO_x layer is followed by an annealing process at a temperature of around 450

°C. Deposition of the thin AlO_x provides field-effect passivation for the rear surface [18].

Rear SiN_x Deposition: Rear side of the PERC solar cell is passivated with AlO_x alongside with SiN_x layer. A plasma-enhanced chemical vapor deposition (PECVD) tool is utilized for the deposition of SiN_x thin film. In this process, optical losses are diminished by reducing the reflection of the rear surface. The refractive index of the deposited SiN_x film and its thickness are the important factors for the rear surface passivation.

Front SiN_x Deposition: Front surface of the solar cell is passivated by SiN_x layer deposited by the PECVD tool. The deposited SiN_x layer on the front surface provides light-trapping ability while reducing the reflection of the sunlight from the surface. Also, it passivates the dangling bonds by hydrogen atoms supplied from the SiN_x layer. The color of the surface is seen as blue since the blue wavelength of the light cannot be absorbed.

Laser Contact Opening (LCO): For the fabrication of metal contacts on the rear side of the solar cell, it is essential to remove the rear stack passivation locally [19]. The localized removal of the passivation stack is generally accomplished by laser ablation. Many parameters can affect the rear side contact formation by laser ablation. These parameters are as follows:

- a) Laser wavelength
- b) Laser pulse duration
- c) Laser frequency
- d) Laser power
- e) Laser beam overlapping
- f) Scan speed

Complementary to these parameters, contact size and contact pitch are the two important parameters for the rear contact characteristics [19].

Therefore, these parameters are optimized in the scope of this thesis study. In the next section 2.3, this process is investigated in detail.

Metallization: This process aims at the formation of front and rear side metal contacts which are the electrodes for the n and p-type surfaces. There are many metallization techniques for the formation of these electrodes. Among all of the metallization steps, screen printing is the most common one due to its convenience for mass production. In this thesis, optimization of the metallization and fast-firing steps will be analyzed thoroughly.

Fast-Firing: The formation of front and rear electrodes is achieved during the fast-firing step which will be applied to a conveyor belt furnace after the metallization process. The solar cell is exposed to a high temperature of up to 750 °C during the fast-firing process. Depending on the temperature and belt speed of the conveyor belt furnace, the characteristics of the solar cell change significantly.

2.3 Laser Contact Opening (LCO) for PERC Solar Cells

In PERC solar cell structure, rear local contact formation is achieved by opening the dielectric layer [20]. Although there are several methods for achieving dielectric opening, the laser contact opening (LCO) method is the most suitable for mass production at the lowest cost. Since the LCO technique is commercially viable, the rear side contact formation design and openings are available for the improvement and should be researched to improve solar cell performance [21]. As a result, the contact formation mechanism, back surface field (BSF) or void generation, and laser parameters that affect the LCO process are all covered in this section.

2.3.1 BSF and Voided Contact Formation Mechanism

The rear side of the wafer is ablated to form the LCOs so that Al-Si local contact formation is achieved at the backside. Since aluminum (Al) paste will be screen-

printed after the formation of the LCOs, printed Al paste will diffuse into the local contacts, and the alloying process starts during the fast-firing process [21]. Aluminum-silicon (Al-Si) alloy formation starts with the melting of aluminum [22]. The specified temperature of melting for the aluminum is around 660 °C. During the alloying process, the silicon spread limit limits the diffusion of silicon into the aluminum matrix [22]. The liquid phase of aluminum diffuses into the local openings of the silicon surface. After that silicon dissolves in the aluminum layer [22]. Since the solubility of silicon in aluminum is higher than the aluminum in silicon, a higher volume of silicon diffuses into the aluminum than aluminum in silicon. Fast-firing temperature determines the diffusion amount and silicon can spread deeper in the aluminum layer depending on the peak temperature of the fast-firing furnace [22]. Figure 2.5 depicts the ultimate state of the alloying process, which includes the formation of the BSF and eutectic area.

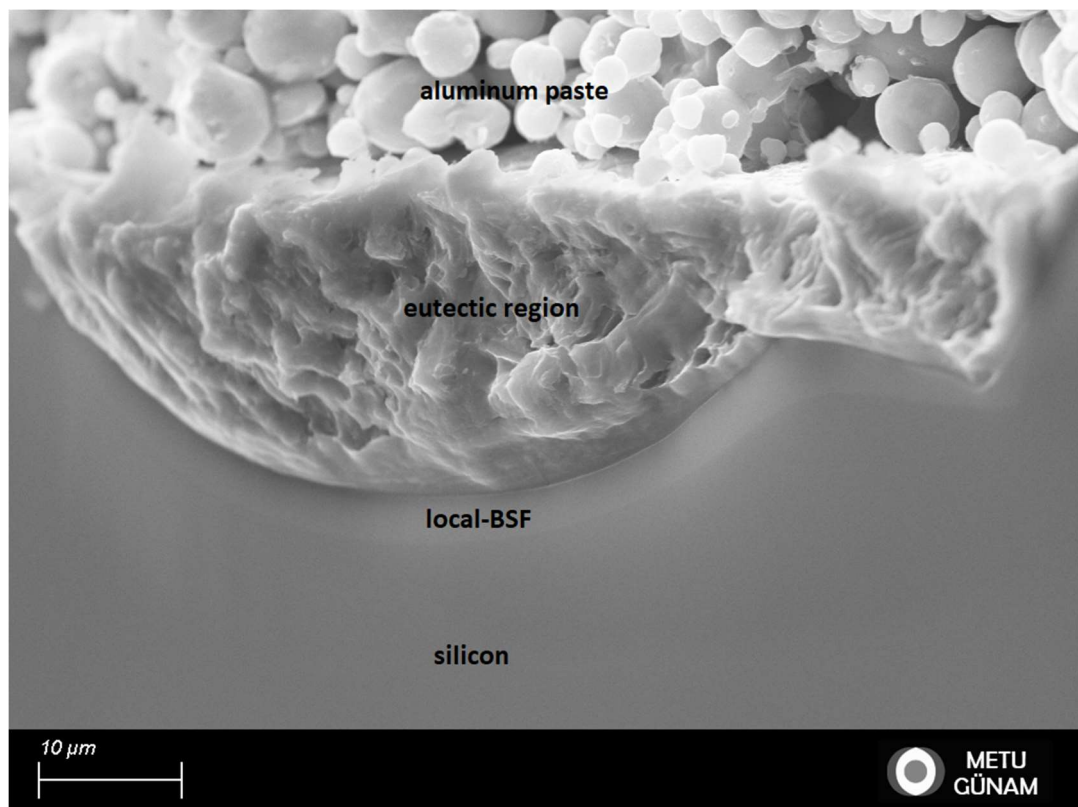


Figure 2.5. SEM image of rear local contact of PERC solar cell

Furthermore, Kirkendall voids, which can be caused by a strong elastic stress field formed in the melt during alloying, are a significant disadvantage of the BSF generation mechanism [23]. Kirkendall effect explains that two types of atoms cannot have the same diffusion rates. In this way, instead of forming a eutectic zone, a large number of vacancies can congregate and generate Kirkendall voids. Figure 2.6 depicts the Kirkendall void formation inside the LCO as seen by SEM.

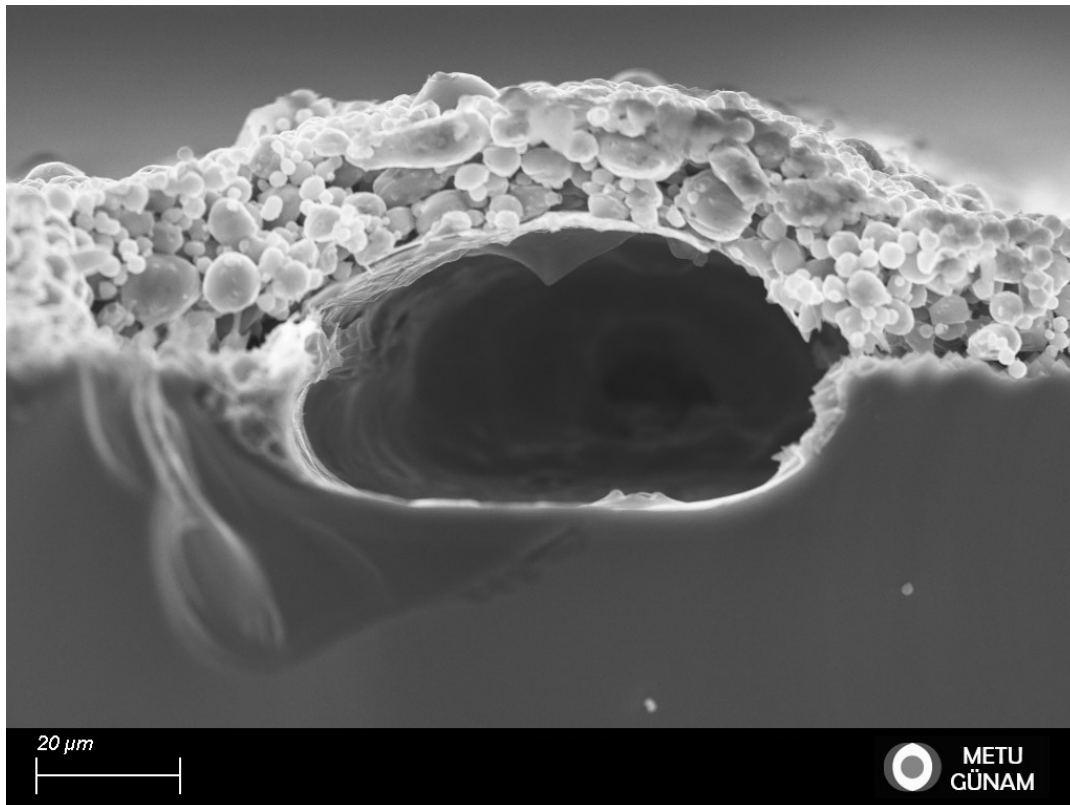


Figure 2.6. Voided contact formation

2.3.2 Laser Parameters

The formation of voided contacts is influenced by several factors. These parameters are given to create a proper contact form on the back side of the PERC solar cell.

2.3.2.1 Laser Power

The most common parameter is the laser power dissipated on the surface. The ablation power should be adjusted to ensure that the contact is well-formed and free of distortion. The laser power also impacts the contact width, which is an essential factor in BSF production. The aluminum paste will not diffuse efficiently through the local contacts if the contact width is too small, resulting in poor contact formation. The rear metal fraction, on the other hand, will be high if the contact width is too high. As a result, the quality of rear passivation will be reduced. As a result, each parameter should be characterized thoroughly to determine the optimal LCO width.

2.3.2.2 Laser Wavelength

The energy levels of photons produced by the lasing material are inversely proportional to the wavelength of the light produced by the lasing material. It means that the shorter the wavelength of light, the higher the photon's energy. Generally, the wavelength of the power source determines the power of the laser beam. Different lasing materials emit light of various wavelengths, resulting in laser beams of varying power levels. The wavelength of the laser should be selected while considering the absorption coefficient and the absorption depth of the silicon since lower wavelengths can be absorbed on the surface. The relation between the absorption coefficient and absorption depth of silicon with wavelength is depicted in Figures 2.7 and Figure 2.8.

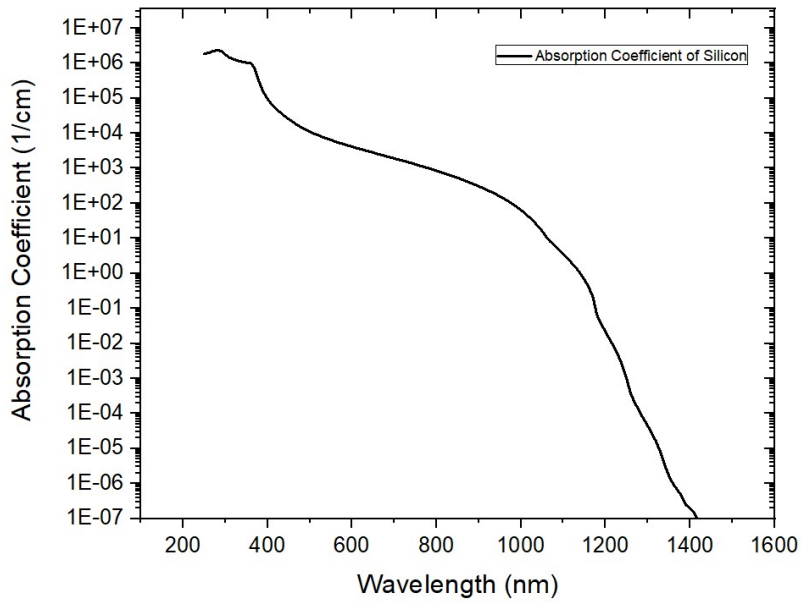


Figure 2.7. Absorption coefficient and wavelength relation of silicon

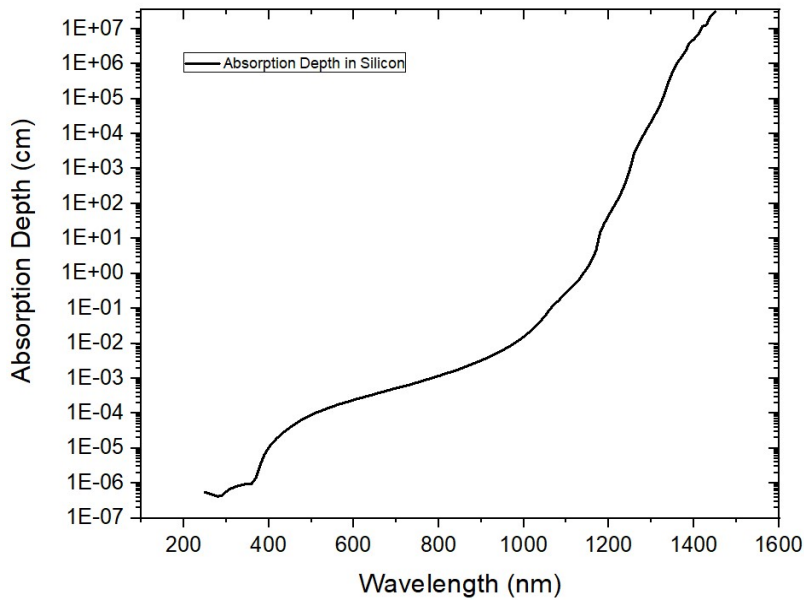


Figure 2.8. Absorption depth and wavelength relation of silicon

Although higher wavelengths can be absorbed in a deeper portion of the silicon, LCO processing requires a moderate wavelength of around 600 nm. Above 600 nm, light can be absorbed more deeply and distort the surface, which is not ideal for LCO.

2.3.2.3 Laser Pulse Duration (Pulse Width)

Laser pulse duration is defined as the time measured over a single pulse at its full width half maximum (FWHM). Short pulses, ranging from nanoseconds to femtoseconds, are required for material processing. Also, peak power obtained from the pulse is directly related to the pulse duration. Pulsed lasers emit a single pulse over a finite period as represented in Figure 2.9.

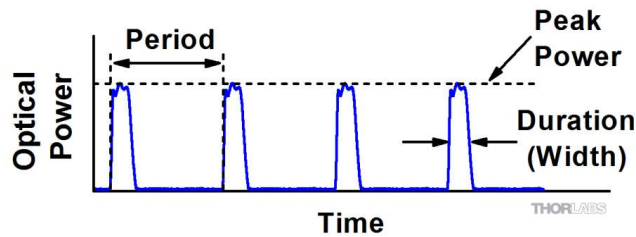


Figure 2.9. Pulsed laser emission representation [24]

2.3.2.4 Laser Frequency

Laser frequency defines the number of pulses emitted from the source in a second.

$$Period = \frac{1}{Frequency} \quad \text{Eq. (2.6)}$$

From Figure 2.9 and Equation 2.6, it can be inferred that a smaller period leads to high frequencies. Hence, many pulses are emitted from the laser source in a second. While the frequency and laser power are strongly associated in material processing, an appropriate frequency value for good contact formation at the back side of the PERC solar cells should be determined.

2.3.2.5 Laser Beam Overlapping

The laser scan speed, operating frequency, and spot diameter of the laser beam directly influence laser beam overlapping. Equation 2.7 explains this relationship [25].

$$Pulse\ overlap = \left(1 - \frac{V}{f * D}\right) \times 100 \quad \text{Eq. (2.7)}$$

V stands for laser scan speed, f for operating frequency, and D for spot diameter at the specified frequency in Eq. 2.7. High overlapping of successive beams might result in more ablation than intended, as well as distortion of the surface. As a result, poor contact formation can happen at the rear side of the PERC solar cells. On the other hand, low overlapping of the successive beams may leave intact regions, where contact formation is impossible.

2.3.2.6 Laser Scan Speed

The speed of the laser scan can be adjusted manually by the operator. It reduces the amount of time the laser pulse is in contact with the surface. At certain frequencies, a slow scan speed may cause the surface to distort. As a result, depending on the procedure, scan speed optimization should be performed using the other parameters listed above. For example, the LCO process requires a high speed of roughly 15 m/s to create a damage-free surface for contact creation.

2.4 Metallization Techniques for c-Si Solar Cells

Crystalline silicon solar cells require metal contacts from the front and rear surfaces so that the connection with the external load is provided. The contact systems of the crystalline silicon solar cells require several properties such as low contact resistivity, good adhesion, and high throughput. There are some methods for achieving solar cell metallization such as screen-printing, electroplating, evaporation, inkjet printing, etc. Among these approaches, some are appropriate for mass production and can achieve high throughput. Each metallization process will be presented in this section, with a special emphasis on screen-printing in Chapter 2.4.5 because it is the basis of this thesis study.

2.4.1 Screen-Printing

Because of its robustness, cost-effectiveness, and high productivity, screen printing is the most widely used metallization technique in the industry. In an hour, an industrial screen printer can print approximately 1500 wafers. With recent innovations in the metal paste market, the width of printed electrodes is gradually decreasing as a means of lowering costs and enhancing cell efficiency. [26]. Figure 2.10 shows the screen-printing process representation.

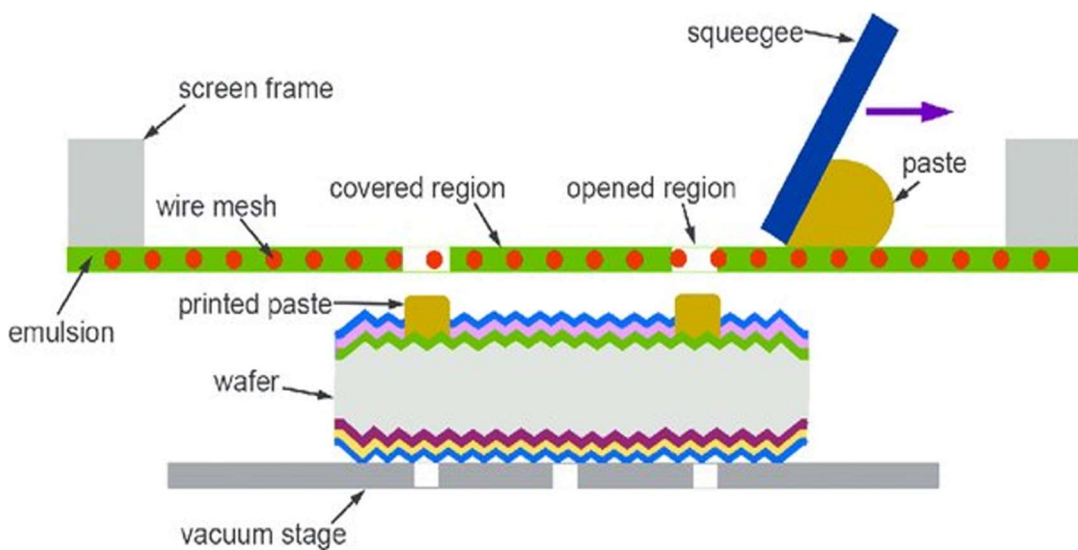


Figure 2.10. Schematic representation of screen-printing process [27]

Different models can be printed on a wafer surface by using specially designed screens and squeegees. The squeegee brings the metal paste onto the screen and then the paste flows through the openings. As a result, the screen pattern is transferred onto the wafer surface. The screen geometry plays a crucial role in the paste transfer, hence, printing quality [28]. Finger width, mesh number, wire diameter, the width of each channel, angle between the finger and mesh, and finger length influence the transfer of paste during the process [29]. All of these parameters can be adjusted during screen production following paste specifications.

Furthermore, other factors affect the printing quality such as squeegee pressure, printing speed, snap-off distance, temperature and humidity of the environment, etc.

2.4.2 Electroplating

Electroless plating is a chemical process that uses chemical reduction reactions and does not require an external potential [30]. A solution that contains reducing agents and metal ions is utilized for the deposition of the ions onto the substrate. Generally, nickel (Ni) is plated electrolessly onto the silicon substrate due to its low contact resistivity and good barrier ability for the diffusion of subsequent copper plating. After that electroplating of copper (Cu) is plated onto the Ni since it is a good conductor.

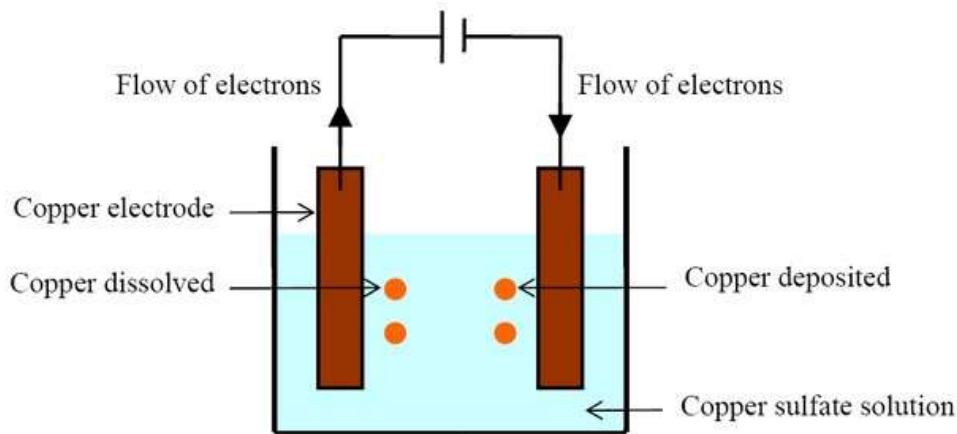


Figure 2.11. Schemical representation of Cu plating

This process is a relatively cheap method of making an electrical contact compared to the other plating techniques [30]. Since electroless plating is a fully chemical process, deposition characteristics and plating rate can be affected by environmental effects such as temperature and pH. In addition, the concentration of the chemical solutions has to be optimized to control the plating process.

2.4.3 Evaporation

Evaporation is a metallization technique that uses vacuum conditions and high temperatures. It is based on the fact that the source material is to raise the vapor

pressure. The material atoms that evaporated in a vacuum environment migrate to the target and adhere to the surface of the source material. There are many types of evaporation such as resistive evaporation, electron-beam evaporation, ion beam evaporation, and inductive heating evaporation.

Since high vacuum conditions are satisfied, this process provides an excellent purity of the film. In addition, the target substrate is not damaged physically. On the other hand, it is difficult to control the film composition and a limited number of the wafers are metalized due to vacuum conditions. Therefore, it is not suitable for mass production.

2.4.4 Inkjet Printing

Inkjet printing is a method that is applied to both organic and inorganic solar cells such as CIGS solar cells (inorganic) and polymer solar cells (organic). Special functional materials are added to the ink depending on the substrate that will be printed. The printing is accomplished by a piezoelectric driver in the nozzle head of the printhead. The programmed pattern is printed onto the surface by several layers. Since the production of PERC solar cells doesn't require this technique, we will not go into detail about this process.

2.4.5 Metallization of PERC Solar Cells by Screen-Printing Method

The screen-printing method is one step ahead of the other metallization techniques described above due to its simplicity and high throughput. Therefore, it is the renowned one among the other techniques. Solar cell metallization by screen-printing requires at least two steps printing of metal pastes, drying, and co-firing to complete contacts. In this sense, this section is devoted to analyzing the screen-printing method in detail with various aspects.

2.4.6 Metallization Screens

Metallization screens are very fine stainless steel mesh items mounted within a frame. They block some areas and leave other areas open where metallization paste can flow.

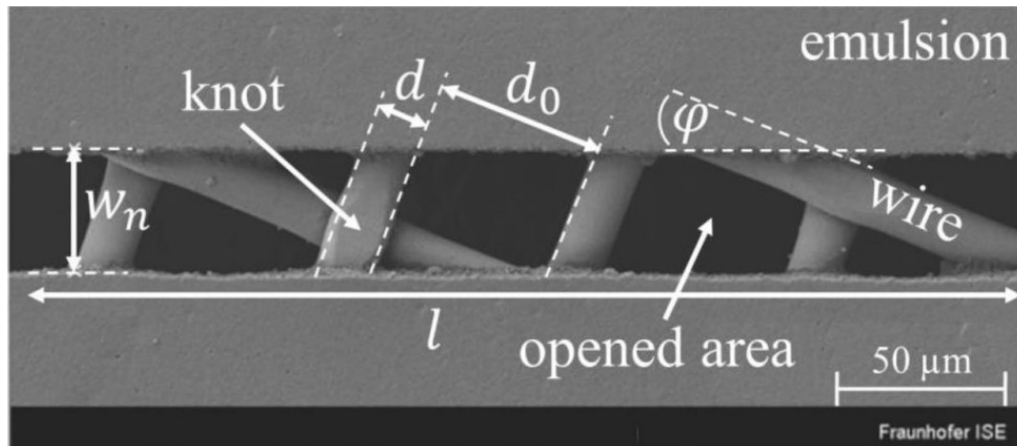


Figure 2.12. Screen opening channel [31]

The mesh count (MC) is a parameter of a screen that improves the fine line printing quality of the metals. For fine line printing, this MC number should be high. In addition, front side silver (Ag) screens have a much finer mesh size than the rear side screens where aluminum (Al) is printed. Wire diameter (d) and emulsion over mesh thickness (EOM) are the other parameters that affect fine line printing. The mesh is made up of stainless steel wires with a diameter that corresponds to the particle size of the paste to be printed. For fine line printing, the wire diameter should be as small as possible. The other important parameter, EOM thickness, is defined as the total stencil thickness minus the mesh thickness. Figure 2.12 shows the other parameters that are necessary for the screen geometry. Screen opening (w_n) is the thickness of the unmasked area, the channel length (l) is the total length of the unmasked area, d is the wire diameter, d_0 is the mesh opening and the angle between emulsion edge and mesh wires is denoted by ϕ [31].

To characterize the geometrical architecture of the screens, some parameters are formulized. The first one is the opening area (OA%). It is defined by the ratio of

opened area to the overall area of one mesh unit. It can be calculated by Equation 2.8 [32].

$$OA \% = \frac{d_0^2}{(d + d_0)^2} \quad \text{Eq. (2.8)}$$

The wire to wire distance d_0 is calculated by Equation 2.9 and describes the number of wires per unit length of the screen.

$$d_0 = \frac{1}{MC - d} \quad \text{Eq. (2.9)}$$

Since screens are exposed to pressure around 80 N, they can be wasted away in time. In other words, an important parameter to provide sufficient printability over the maximal possible screen life cycle is denoted as the screen tension (γ_{screen}). The screen tension is given by Equation 2.10.

$$\gamma_{\text{screen-max}} = \sigma_{\text{uts-wire-mat}} MC \pi \frac{d^2}{4} \quad \text{Eq. (2.10)}$$

The first parameter ($\sigma_{\text{uts-wire-mat}}$) is a material parameter that describes the minimal stress which is necessary to break the material while it is stretching. It is known as ultimate tensile strength and this number is unique for each material.

2.4.7 Solar Cell Pastes

In silicon solar cells, the formation of good ohmic contact between metal and emitter with minimum specific contact resistivity is crucial for obtaining high electrical performance. Many parameters affect the contact quality such as paste chemistry and process conditions.

Solar cells are metalized with aluminum and silver paste depending on the type of the solar cell structure. For PERC solar cells, the rear side is screen-printed with aluminum paste, and the front side is screen-printed with silver pastes. Since different pastes are used, there is a need for different screens for each printing.

Therefore, depending on the printing method, the paste type, and their composition change.

An example of the aluminum paste matrix composition is Al powder, aluminum oxide powder, ethanol, α -terpineol, and ethylcellulose [33]. The laser openings at the rear side of the PERC solar cell are filled by the Al paste and local back surface field formation is achieved.

The front side of the PERC solar cell requires at least one step of screen printing. The silver (Ag) paste is printed on the front surface and the pastes are varied depending on the printing type. The details about printing methods will be given in section 2.4.8. The composition of the silver paste mainly includes silver particles, glass frit, and solvents. Therefore, the screen-printing process has to be done in a temperature and humidity-controlled environment.

In this thesis, aluminum paste supplied from the Toyo-Al firm is printed on the rear side of the PERC solar cells, while the front side is printed by Heraeus Photovoltaics and Pharos Materials silver pastes. To obtain high performance from the screen printing, a fast-firing recipe has to be developed for each paste. Since each paste has a different fast-firing temperature window, an investigation of fast-firing will be done thoroughly in Chapter 3.

2.4.8 Screen-Printing Methods and Parameters

Metallization of the solar cells requires at least two-step printing. Generally, the whole rear surface of the PERC solar cell is printed by Al paste. For module applications, Ag busbar pads are also printed on the rear surface. To accomplish the front surface metallization, the screen-printing technique has three well-known methods to form the metal contacts with the underlying substrate. These methods are as follows:

1) Single-printing: In this method, a single type of conductive silver paste is printed through the metallization screen to form the front side electrodes. During the single

printing process, small current collectors (fingers) and large current collectors (busbars) are printed simultaneously. After the drying process, they all co-fired in a conveyor belt furnace.

2) Double-printing: In this method, front surface electrodes are printed firstly by contacting paste, and then the same electrodes are printed once more by conducting paste. Although this method was too popular until a few years before, it is phased out due to the recent developments in screen and paste markets.

3) Dual-printing: In this method, front surface electrodes are printed in two steps by using two different Ag pastes. Firstly, busbars are printed with specially designed conductive paste. The ingredients of this paste differ from the paste that fingers will be printed after this step. Therefore, two different screens are used for the printing of the front surface electrodes. Figures 2.13 and 2.14 show these screen layouts drawn by using a CAD program.

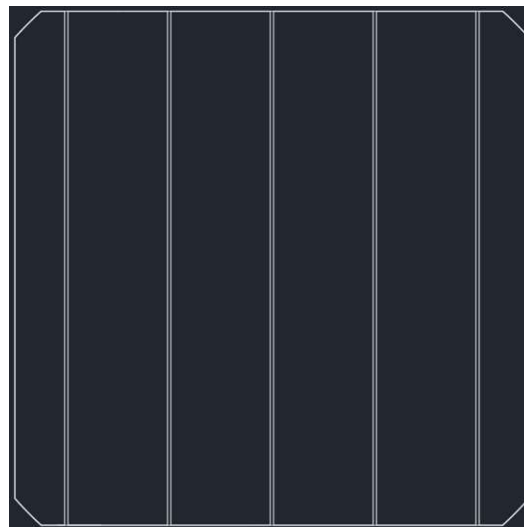


Figure 2.13. CAD drawing of busbar screen

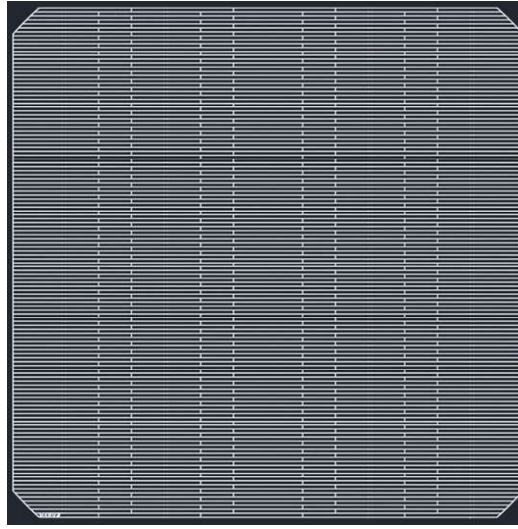


Figure 2.14. CAD drawing of fingers screen

During all three printing methods, there are common printing parameters that are crucial for obtaining the best printing quality. These parameters can be controlled by the user.

a. Snap-off distance: The distance between the screen and the wafer is specified by snap-off distance. It facilitates the release of the paste from screen openings and it can provide a high aspect ratio.

The aspect ratio is a measurement of the printed electrode's height to width ratio. It will be explained in the next section.

b. Squeegee pressure: The squeegee applies a force while it is sweeping the paste onto the screen. Too much pressure may damage the screen and the printing quality will be poor. Too low pressure may yield disconnections on the electrodes. Therefore, this parameter should be optimized depending on the process conditions.

c. Printing speed: Sweeping the paste onto the screen is sensitive to the printing speed of the squeegee to avoid disconnections on the printed metals.

d. Flood speed: It is a speed that which the remaining paste is pulled back to the initial position via flood.

After the screen-printing process, drying furnaces are utilized so that the aluminum and silver pastes are dried individually. The drying process requires a furnace that

has 3-4 zones with different zone temperatures around 150-200 °C. After the drying process, samples are fired on a conveyor belt furnace which has 6 zones with a peak temperature of around 850 °C.

2.4.9 Aspect Ratio

Since fine line screen printing is targeted, the printed fingers have to be as narrow as possible while their height is maximized. Therefore, the cross-section of the printed fingers will be imaged and the dimensions will be measured. Scanning electron microscopy (SEM) will be utilized for the measurement of the dimensions. Figure 2.15 is an SEM image in which the aspect ratio can be calculated by using the measured dimensions.

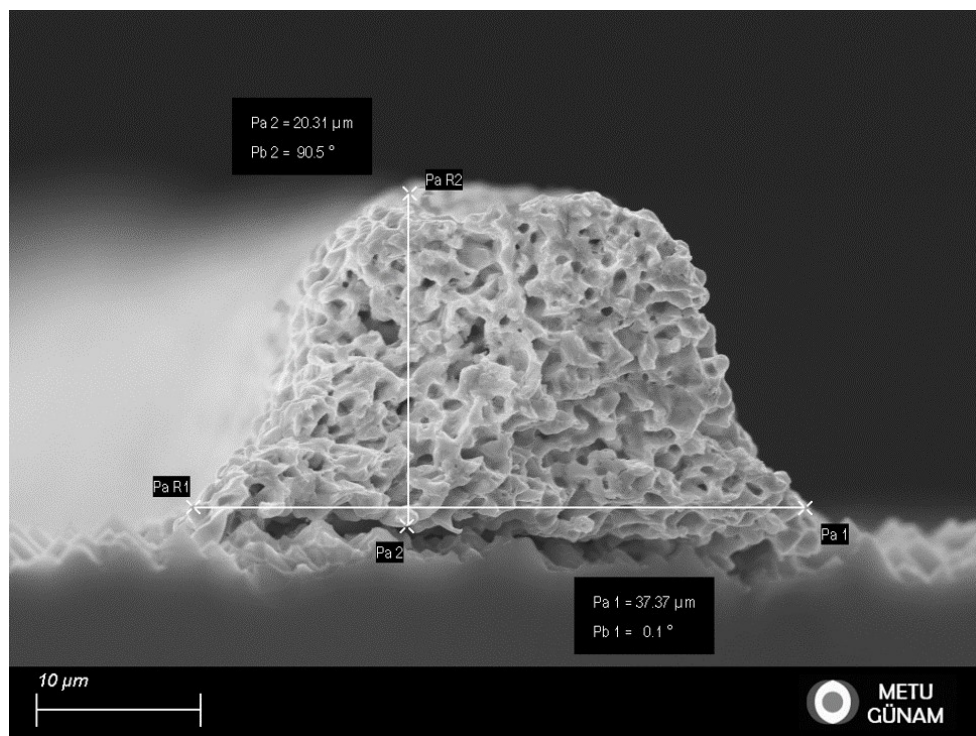


Figure 2.15. Cross-section view of a finger

2.5 Resistive Losses

The cumulative resistive losses in a solar cell are defined as a characteristic resistance (R_{CH}). It is the output resistance of a solar cell at its maximum power point. An I-V curve of a solar cell is shown in Figure 2.16, which can be used to calculate the characteristic resistance.

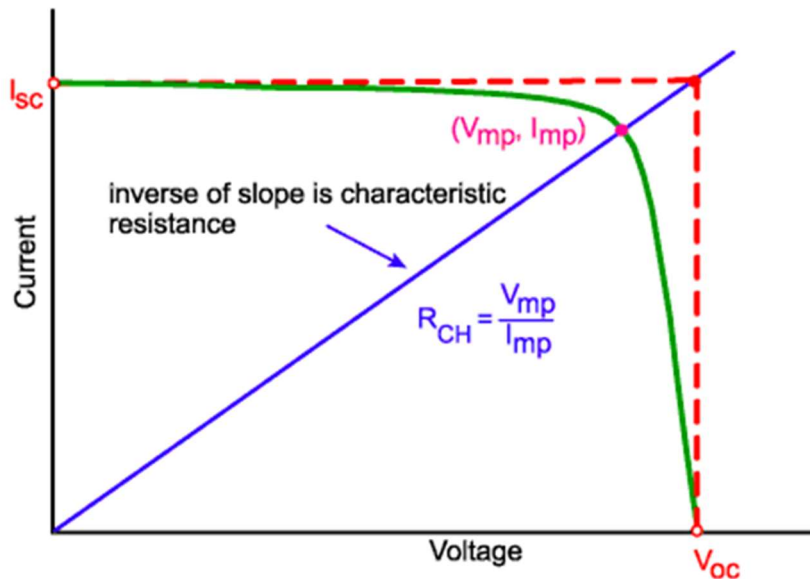


Figure 2.16. An I-V curve of a solar cell [34]

The inverse slope of the blue line gives R_{CH} of the solar cell. It has a unit of Ω (Ohms).

2.5.1 Series Resistance (R_s)

The series resistance of a solar cell is an ohmic resistance that appears in a solar cell and it degrades the FF of the device. Figure 2.17 shows the resistances that constitute the R_s .

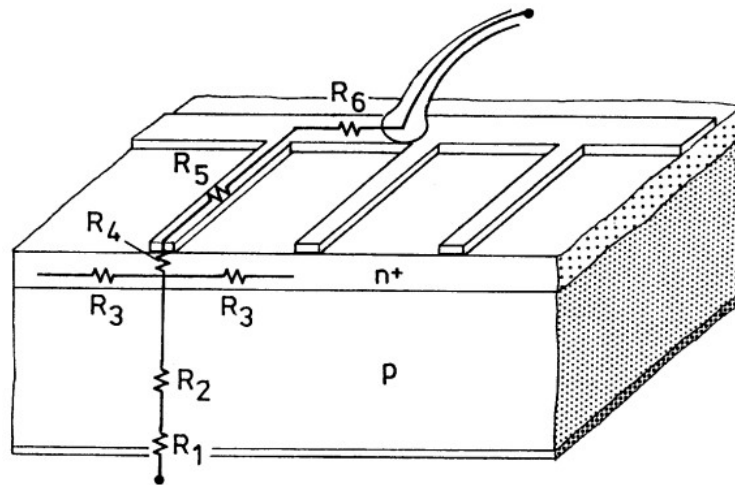


Figure 2.17. Resistances that constitute the R_s [35]

The shown resistances are as follows: R_1 is the resistance between metal-semiconductor contact on the total back surface, R_2 is the base resistance, R_3 is the emitter resistance between two metal fingers, R_4 is the metal-semiconductor contact resistance, R_5 is the finger resistance and R_6 is the busbar resistance [35].

The influence of the R_s on the I-V curve of the solar cell is shown in Figure 2.18.

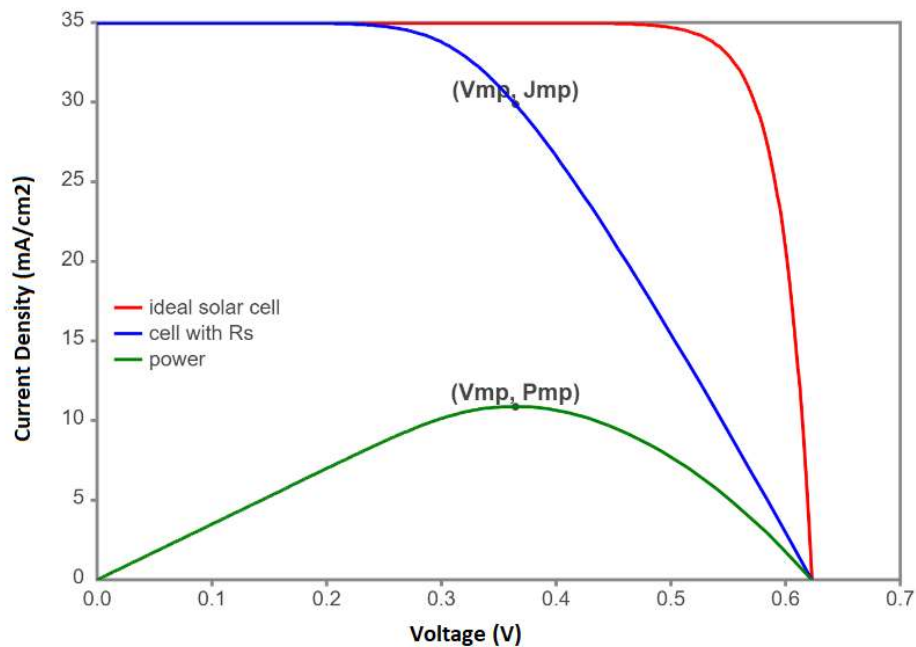


Figure 2.18. Effect of high series resistance on the solar cell I-V curve

As shown in Figure 2.18, the expected (ideal) I-V curve of a solar cell should be the red curve. The curve, however, bends like the blue one due to the high series resistance.

R_5 and R_6 can be measured by the line resistance measurement method, but the Transmission Line Measurement (TLM) tool will be utilized for the measurement of the R_4 . The details of the TLM tool will be given in Chapter 3.

2.5.2 Shunt Resistance (R_{sh})

The magnitude of the shunt resistance is an indicator of the current leakage from the solar cell. The source of this current leakage may be the edges of the solar cell or point defects in the p-n junction. These defects lead to the interruption of the p-n junction. They originate during the diffusion of the emitter such that impurity particles can behave as a barrier for diffusion at some points. In addition, base material (silicon) may also be contacted with metal contacts. Therefore, a short circuit is created which creates a current leakage from the device. To lessen the negative effects of the R_{SH} on the solar cell, its magnitude should be high. Figure 2.19 shows the I-V curve that has low R_{SH} .

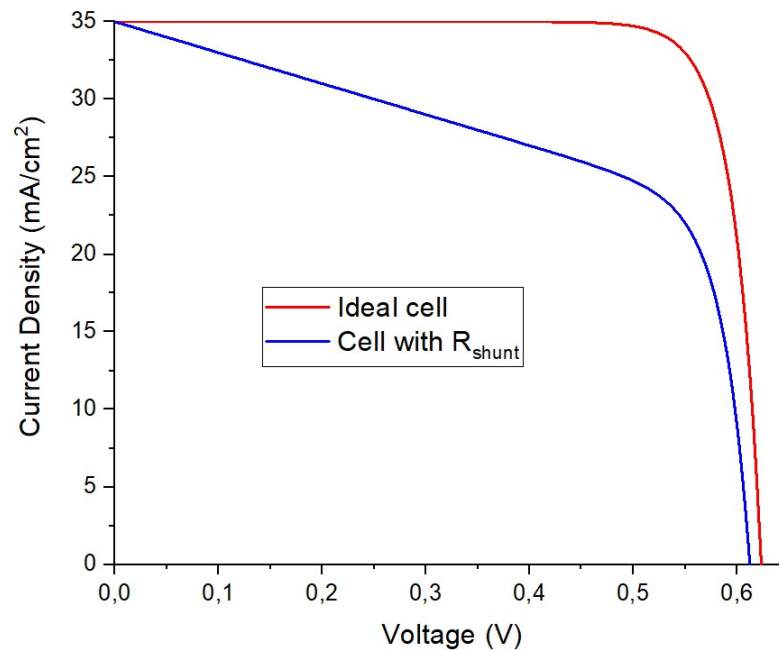


Figure 2.19. Effect of low shunt resistance on the solar cell I-V curve

As shown in Figure 2.19, the solar cell I-V curve (blue) deviated too much from the ideal cell curve (red).

2.5.3 Contact Resistance (R_c)

Contact resistance (R_4 in Figure 2.17) appears between fingers and the emitter region. It is expected to be as low as possible since it degrades the FF due to an increase in R_S . To decrease the R_c , the emitter should be heavily doped. If heavily doping is satisfied (emitter sheet resistance is low), good contact formation can be achieved due to the increased conductivity of the emitter. However, a high amount of diffusion brings other problems. For instance, an excess amount of phosphorus creates a dead layer on the emitter surface which drops the possibility of collecting light-generated carriers.

Reducing the contact resistance can be achieved via the selective emitter formation by the laser doping method. The selective emitter concepts have gained great interest since energy conversion efficiency can be increased by more than 0.3%_{abs}

in the passivated emitter and rear solar cell (PERC) technology compared to homogenous emitter [1-2]. The gain in the selective emitter is mainly due to the reduced emitter dark saturation current density of passivated emitter regions $j_{0e,pass}$, which is possible with lower surface doping concentration [3-4]. On the other hand, the emitter regions under the metal contacts should be heavily doped for a lower saturation current density of the metalized region, $j_{0e,met}$ [2-4-5]. Also, heavily doped areas yield minimal specific contact resistivity (ρ_c), which is desirable for low series resistance in a solar cell.

The contact quality is greatly influenced by the fast-firing process. Superior contact quality can be achieved by optimizing the temperatures of the fast-firing furnace.

2.6 Optimization of Front Grid Design

Resistive losses due to the front metals should be minimized to obtain a low R_s . Therefore, optimization of front grid design has a profound impact to reduce the resistive losses in a solar cell. In this thesis, front grid optimization is done by using the program “GriddlerPro”. It allows us to design and simulate a variety of solar cells using the inputs provided.

The Griddler Pro program is utilized to determine the optimal front metal fraction. While specifying the metal fraction, the number of fingers and busbars, the width of each finger, and other dimensional parameters are extracted from the simulation results. Thus, the best metallization screen design can be chosen for the solar cells that will be fabricated.

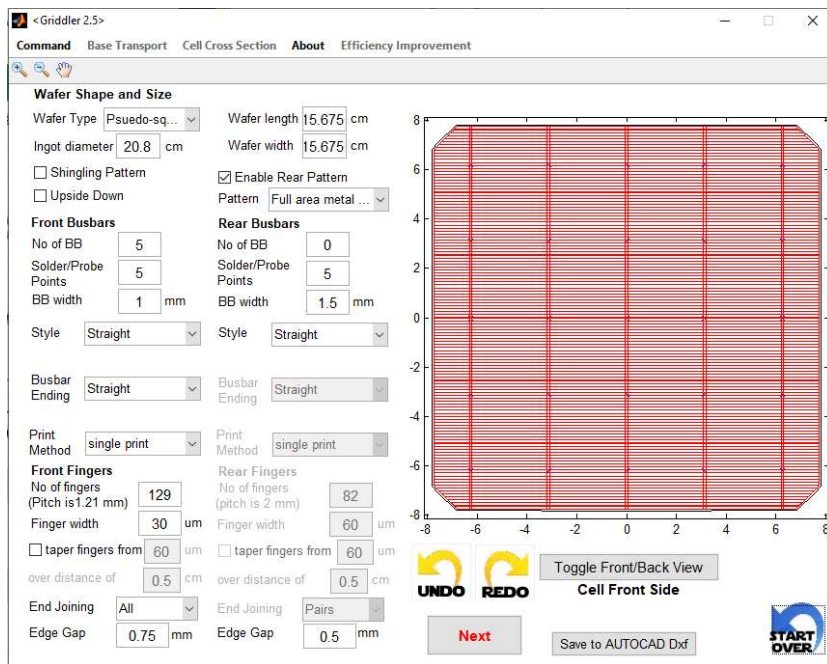


Figure 2.20. Griddler input screen for wafer shape and size

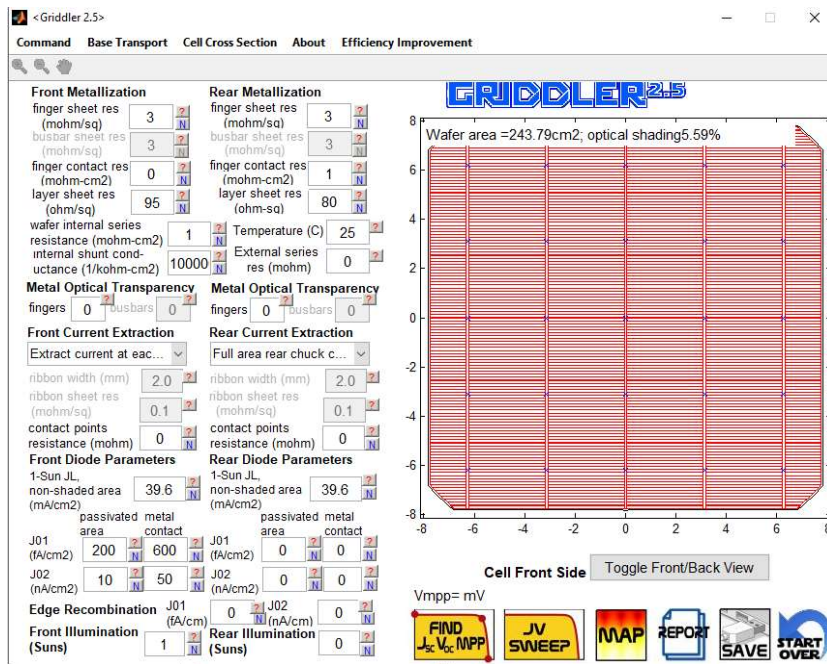


Figure 2.21. Griddler input screen for front and rear metallization parameters

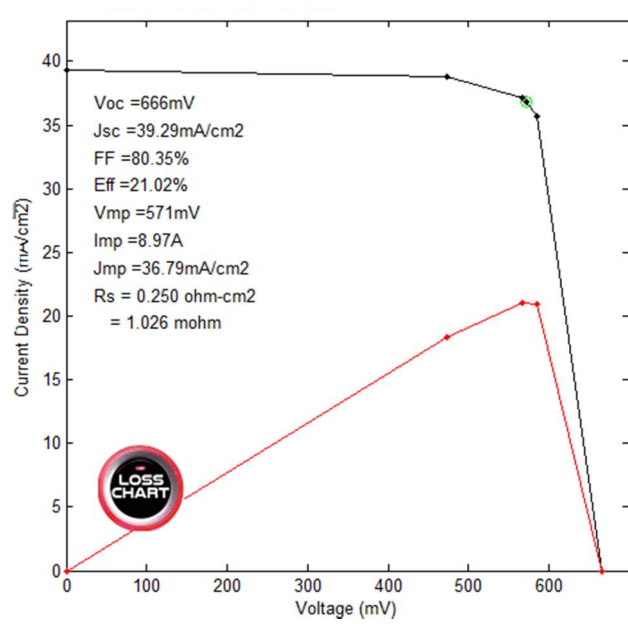


Figure 2.22. An example of a Griddler simulation result

The Griddler simulation results will be introduced in Chapter 4.

CHAPTER 3

EXPERIMENTAL DESIGN AND PROCEDURES

In this study, the experiments are designed using production tools such as a laser system, metallization line, and fast-firing furnace. In addition, characterization tools such as solar simulator, transmission line measurement setup (TLM), scanning electron microscopy (SEM), electroluminescence (EL) imaging, photoluminescence (PL) imaging, line resistance measurement setup, and dark I-V measurement setup are also utilized for the necessary characterizations. This chapter is devoted to the experimental design and the optimizations that will be carried out.

3.1 Production Tools and Experimental Design

3.1.1 Innolas Laser System

The industrial-sized laser system which has a picosecond (ps) pulse width is designed for micro-material processing that is also suitable for photovoltaic applications. By choosing a suitable chuck, 156 mm² and 156.75mm² size wafers can be processed in our system. The system is run by CNC (Computer Numerical Control) and PLC (Programmable Logic Controller). As a laser source, Coherent Hyper Rapid 25 HE that emits short pulses around 10 ps at a 1064 nm wavelength regime with high pulse energy is used. The wavelength of the laser source can be changed to 532 nm (green) wavelength as well. The system provides a wide repetition rate frequency window from 200 kHz to 1 MHz. In addition to those, beam scanning speed can be varied from 0.01 m/s to 15 m/s.



Figure 3.1. InnoLas laser system

3.1.1.1 Experimental Procedure for Rear LCO and Metallization

The rear dielectric passivation stack layers of p-type mono c-Si Czochralski wafers of M2 size were ablated by laser to create local contact openings for PERC cell fabrication. The dash patterns were formed with fixed laser contact opening (LCO) width by the InnoLas laser system. In this study, the laser power of 11.6 W was used which was optimized in another Master of Science thesis [41]. By using that power value, the rear side metallization fraction which has a vital role in the rear side passivation quality was optimized. This optimization is started by studying the rear local contacts of the PERC solar cells in terms of contact patterns, and contact pitches; hence, metallization fractions. The rear dielectric passivation layer was ablated with 3 different dashed line designs (1:1, 2:1, 3:1). Each of the dashed lines has 4 different contact pitches in the order of 900 μm , 1000 μm , 1100 μm , and 1200

μm ; hence, metal fractions of 3.54%, 3.19%, 2.90%, 2.64%, respectively. The line pattern was kept as a reference which has a 1500 μm contact pitch and 4.20% metal fraction on the rear side of the PERC solar cell. The dash length, dash width, and the distance between two successive dashes were kept constant at 650 μm , 60 μm , and 650 μm , respectively for each pattern.

Figure 3.2 represents the rear LCO patterns for both straight lines and dashed lines.

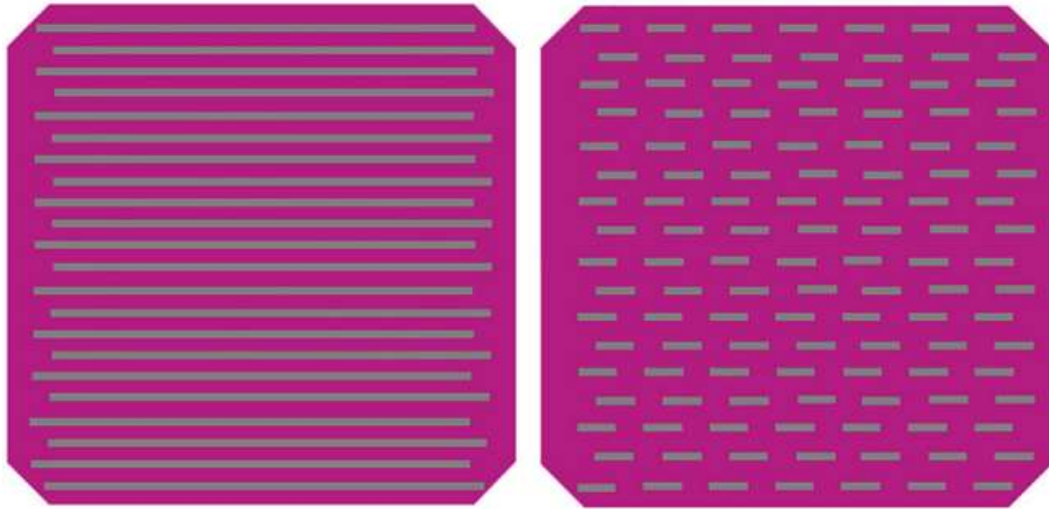


Figure 3.2. Straight line and dashed line patterns for rear LCO [42]

After the ablation, implied open-circuit voltage (iV_{oc}) values were measured with the quasi-steady state photoconductance (QSSPC) method by the Sinton tool after the fast-firing process. These results were correlated with photoluminescence (PL) images. Then, Al paste was screen printed on top of the rear surface in a different group of wafers, and the samples were fired on a conveyor belt furnace. Cell performances were obtained by current-voltage (I-V) measurements with a class AAA solar simulator under the standard test conditions. Produced solar cells are characterized by SEM in terms of void or BSF formation inside the rear local contact openings. The photovoltaic parameters, especially V_{oc} and FF, are correlated with the void analysis. The results will be presented in the next chapter.

3.1.2 Baccini Screen-Printer

The ODTÜ-GÜNAM PV line includes a high-throughput screen printing process for solar cell production. This line includes three printers and three drying ovens. The Baccini screen-printer makes the metallization process more efficient as it can print roughly 900 wafers per hour.



Figure 3.3. Baccini metallization line at ODTÜ-GÜNAM

The control panel can be used to manually adjust printing parameters for an ideal process. Wafers are carried to the oven via the walking beam mechanism after the printing step. The oven is divided into four zones, each with a temperature range of 150 to 200 °C. Inside the oven, printed wafers are dried for 10 minutes before being transferred to the other printer along the walking beam axis.

For the metal contact formation of the PERC solar cells, we use at least two printers, one for rear aluminum contacts and the other one for the front silver contacts. With the recent developments in the paste industry, there is an option to print fingers and busbars separately (see Chapter 2.4.8). Therefore, we use the third printer if the dual printing option is chosen. There are some drawbacks of the dual printing such as misalignment, poor adhesion of busbars, different fast-firing windows of finger and busbar pastes, etc.

The Baccini screen printers are operated with optimized printing parameters. These parameters were explained in Chapter 2.4.8. Optimization of the printing parameters will be presented in the next chapter.

3.1.2.1 Experimental Procedure for Front Surface Metallization

Figure 3.4 depicts the screen design approach for the optimum solar cell characteristics as well as the plan for its integration into the process. Commercially produced blue wafers (processed up to LCO) are used for this experiment.

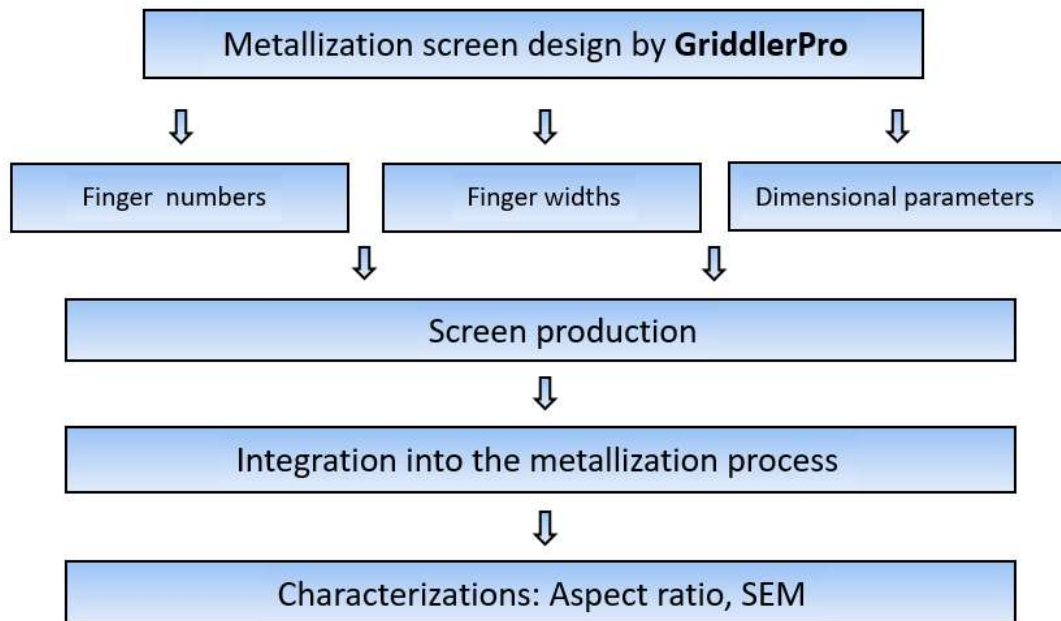


Figure 3.4. The plan for the screen design experiment

The goal of this experiment is to improve the physical properties of the front surface metallization screen, which has a significant impact on the cell structure. Less shadowing is targeted by optimizing the Ag screen design. The integration of the produced screen into the processes is done by utilizing two different Ag pastes supplied by Heraeus PV and Pharos Materials after screen manufacture. The ideal aspect ratio for each type of Ag paste is calculated by adjusting the parameters of the screen-printer.

3.1.3 BTU Fast-Firing Furnace

Screen-printed aluminum and silver pastes are co-fired on a conveyor belt furnace for the front and rear contact formation. Therefore, BTU fast-firing furnace in the ODTÜ-GÜNAM laboratories is used. This furnace can reach up to 950° C and the belt speed can be increased up to 1000 cm/min.



Figure 3.5. BTU fast-firing furnace in ODTÜ-GÜNAM laboratories

The fast-firing process is highly crucial for achieving high-efficiency solar cells. Therefore, the fast-firing process is studied thoroughly in the scope of this thesis.

3.1.4 Experimental Procedure and Details for the Fast-Firing Recipe Development

The second design of the experiment aims the determination of the best matching fast-firing recipe with the two types of Ag pastes used in the first experimental plan.

The fast-firing profiles of two well-known companies, Heraeus PV and Fraunhofer ISE are analyzed. The datasheet of the Ag paste from Heraeus PV provides recommended fast-firing profile and that profile was digitized as a function of time. Also, in [43], Fraunhofer ISE and BTU collaborated on work and provided their fast-firing profile. As a function of time, that profile is also digitized. To make adjustments, the two profiles are compared to the present fast-firing profile of us measured with the Datapaq 900. Figure 3.6, Figure 3.7 and Figure 3.8 indicate profiles of the Heraeus PV, Fraunhofer ISE and ODTÜ-GÜNAM, respectively.

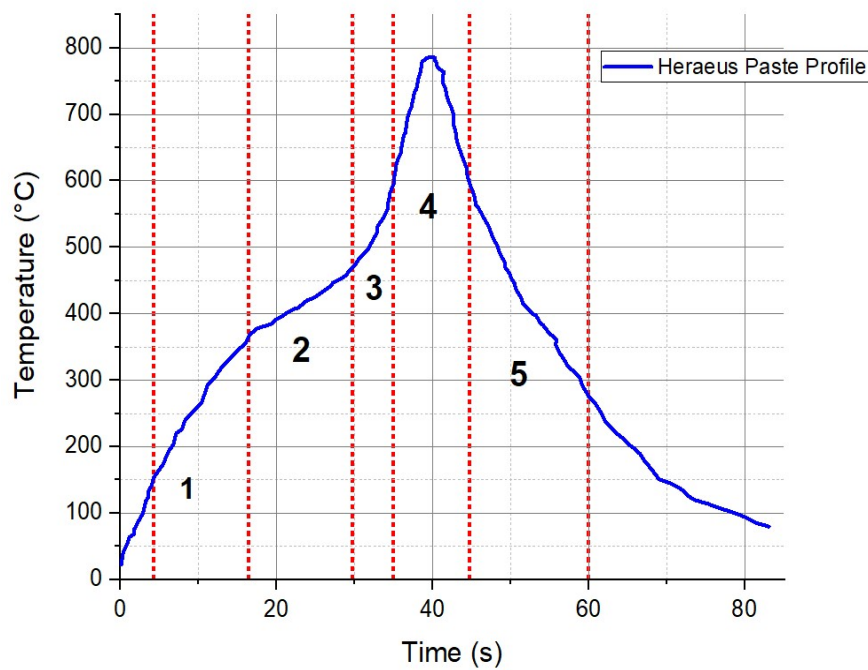


Figure 3.6. Fast-firing profile of Heraeus PV

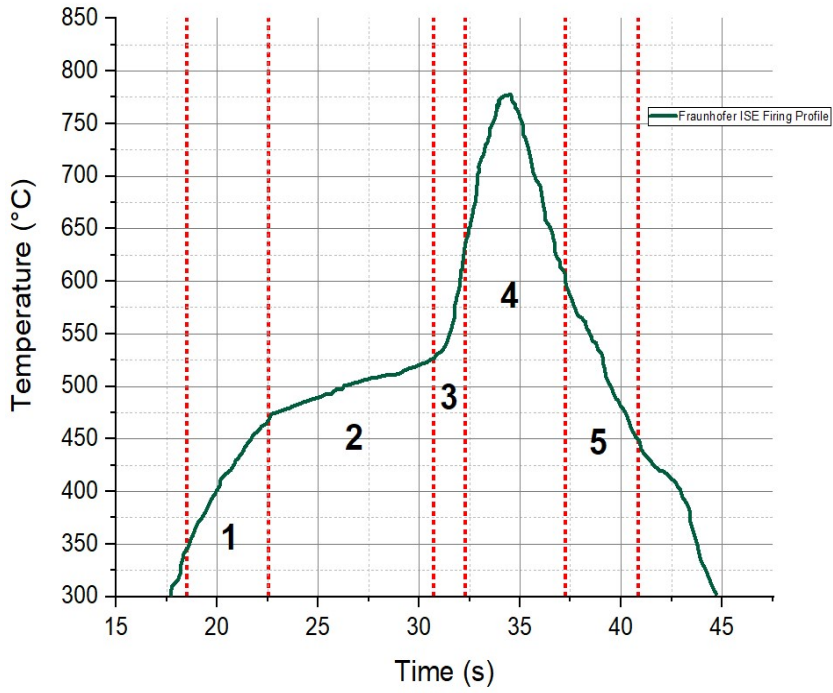


Figure 3.7. Fast-firing profile of Fraunhofer ISE

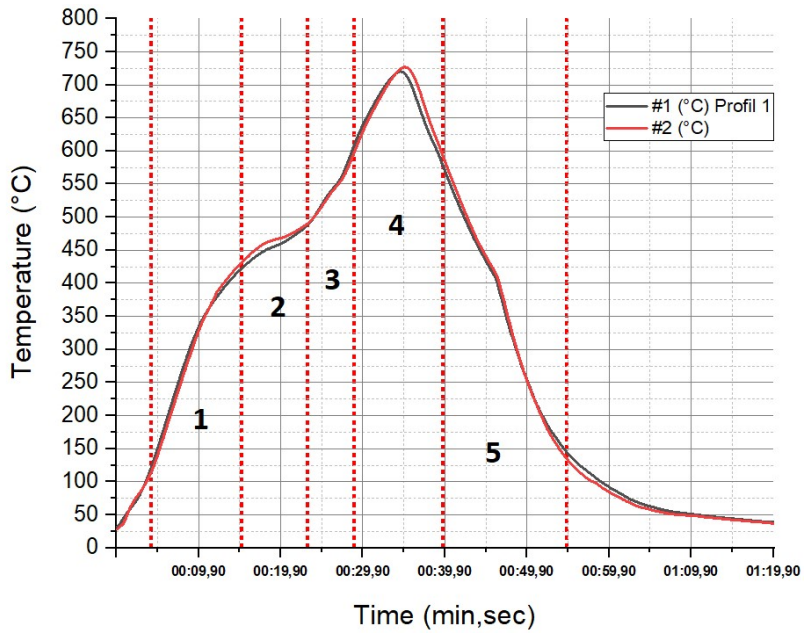


Figure 3.8. Standard fast-firing profile of ODTÜ-GÜNAM

First, blue wafers were employed to develop the best matched fast-firing profile on the produced solar cells in ODTÜ-GÜNAM. In terms of bulk characteristics, doping profile, passivation quality, and so on, these wafers are remarkably similar to ODTÜ-GÜNAM wafers. These blue wafers were processed up to the LCO, and the LCO, metallization, and fast-firing processes were completed at ODTÜ-GÜNAM. The use of blue wafers ensures that consistent results can be obtained on identical wafers.

The fast-firing profiles are divided into five regions. Depending on the temperature zone, these regions determine specific processes. The regions are described here, along with their contribution to the fast-firing profiles.

- 1- Organic binders and solvents are fired during this region. This region is called as “First ramp rate”.
- 2- This region determines the plateau region where Al starts to melt and the formation of the eutectic region starts. In addition, it was observed that SiN_x layer is etched by a glass frit in this region.
- 3- This region plays a crucial role in the formation of the eutectic region. Also, front surface metal contact is started.
- 4- For a good metal contact formation on the front side of the solar cell, the time interval above 600 °C is an important parameter. Therefore, the time interval is measured during the 4th region. Too much time above 600 °C may cause shunt resistance while less time results in poor contacting.
- 5- BSF formation is completed during the cooling part of the fast-firing process.

The analysis results will be presented in Chapter 4.

Two different Ag paste brands, Heraeus Photovoltaics, and Pharos Materials are compared and characterized in terms of contact resistivities, series and shunt resistivities, aspect ratios, line resistivities, and sintering quality. In addition, solar cells are metalized with these paste brands, and the PV parameters are compared to produced solar cells.

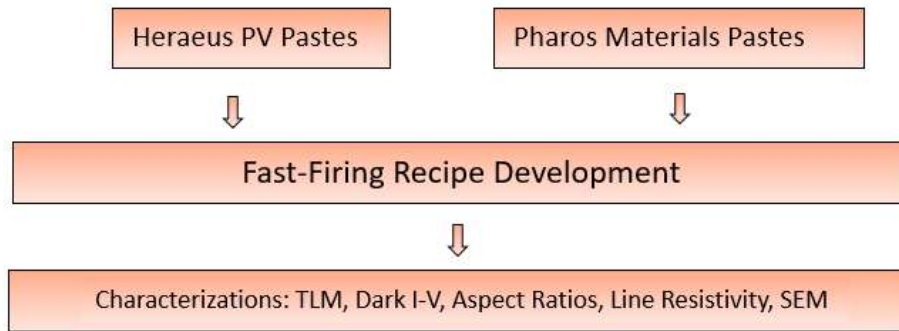


Figure 3.9. Design of the experiment for fast-firing recipe development

3.2 Characterization Tools

3.2.1 Solar Cell Tester and Sorter

ODTÜ-GÜNAM PV line use AAA class solar cell tester and sorter for the measurement of the PV parameters and the efficiency of the solar cells. This tool is calibrated before each measurement with a calibration cell certified by Fraunhofer ISE CalLab.

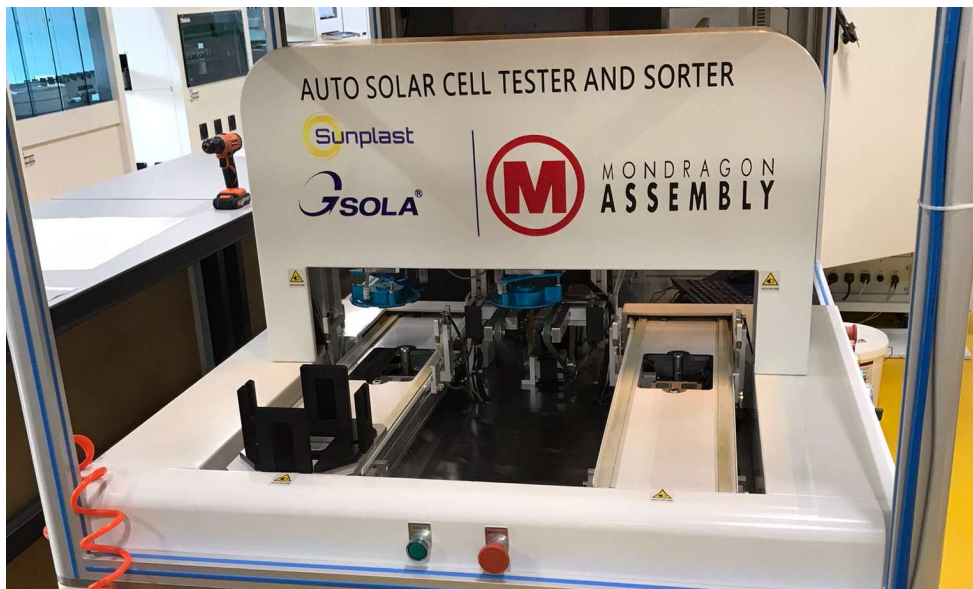


Figure 3.10. Solar cell tester and sorter in ODTÜ-GÜNAM laboratories

It measures the PV parameters by an instant flash that is equal to 1-sun illumination. The reference I-V result from the cell tester is shown in Figure 3.11.

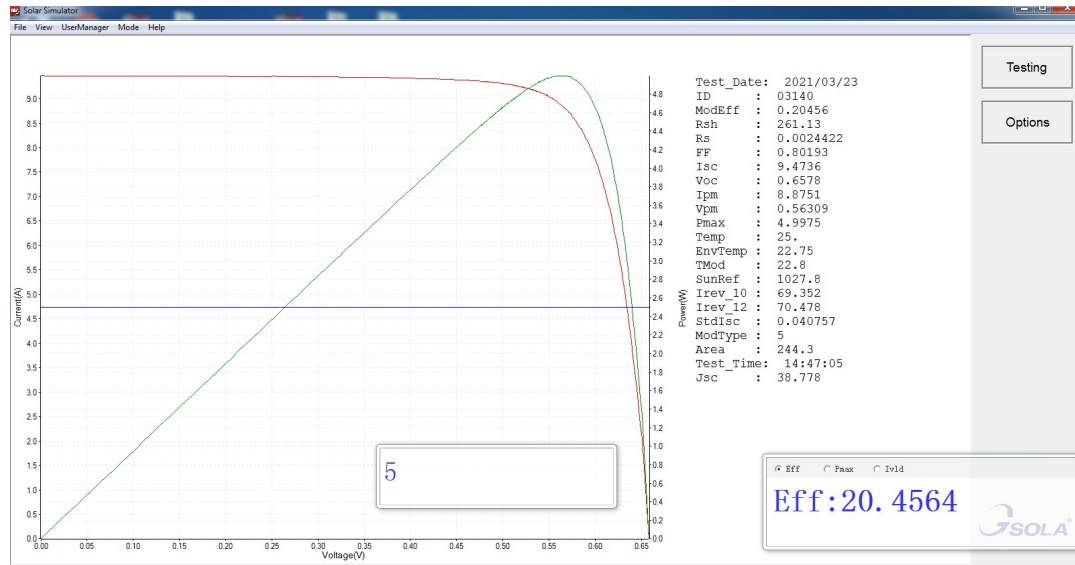


Figure 3.11. Reference solar cell I-V result taken from solar cell tester and sorter

3.2.2 Transmission Line Measurement (TLM)

TLM extracts the contact resistance (R_C) and contact resistivity (ρ_C) from a finger grid structure. The classic TLM structure consists of parallel contact fingers with equal width. However, the fingers are separated by varying distances from each other.

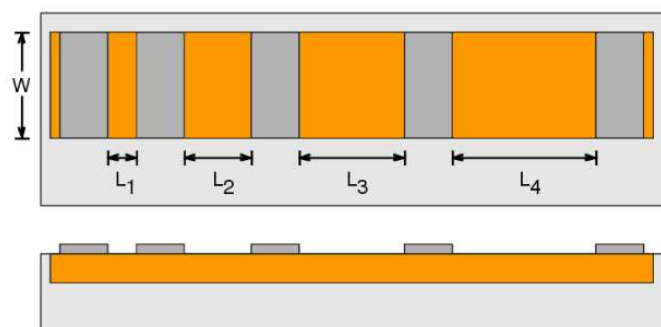


Figure 3.12. Top and side view of the schematic representation of TLM structure [44]

The emitter sheet resistance of the wafer is assumed to be the same everywhere. Then, the resistance between two neighboring fingers is calculated by Equation 3.1. [44]

$$R_{1,2} = 2R_c + \left(R_{sheet} \frac{L_1}{w} \right) \quad \text{Eq. (3.1)}$$

Linear regression of the measured resistances vs. distances gives R_c from the intercept. In addition, the slope of the line gives the R_{sheet} .

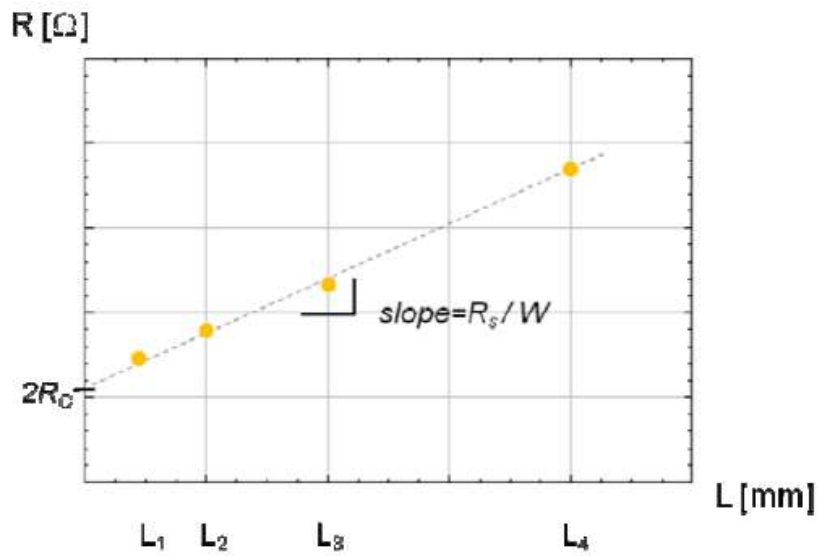


Figure 3.13. Resistance vs. length graph [44]

3.2.3 Line Resistance Measurement

Line resistance measurement is applicable for fingers and busbars. The resistance can be determined with a test structure or piece of the solar cell where single fingers have been electrically isolated. The length of the finger that will be measured should be as large as possible and the test current should be kept at a maximum for an accurate measurement [44]. In this thesis, reducing the line resistance is aimed to increase current carrying.

3.2.4 Scanning Electron Microscopy (SEM)

Topography and composition information can be gathered via SEM [45]. A sample is scanned with a focused electron beam and the necessary information is obtained. Figure 3.14 shows the components of the SEM with a secondary electron detector that collects the electrons scattered from the sample. Since the system works under vacuum conditions, it acquires a high-resolution image.

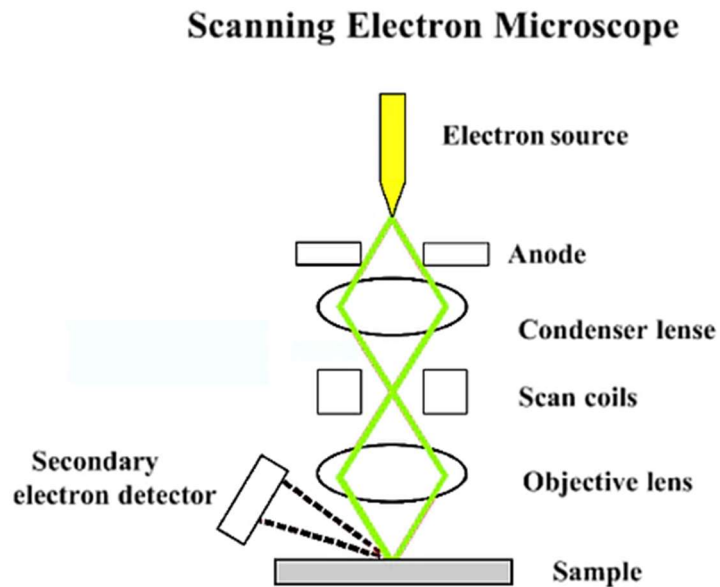


Figure 3.14. Components of SEM [45]

In this thesis, SEM is usually used for monitoring the back surface field or void formations inside the LCOs. In addition, the aspect ratio of the front fingers is calculated by using the SEM.

3.2.5 Electroluminescence (EL) and Photoluminescence (PL) Imaging

EL and PL imaging are the two types of luminescences. They are similar characterization methods that make a visual inspection. The surface of the sample is excited to emit luminescence and the image is acquired via a camera. Both techniques have some specific usages. For instance, EL needs contact with the

sample since current is passed these contacts through the sample. On the other hand, PL uses optical excitation and avoids contact with the sample. Therefore, it protects the sample from mechanical damage as well as shadowing problems during the measurement [46]. In addition, lifetime mapping of the samples can be done via PL.

In this thesis, PL is used for the characterizations of the rear LCOs.

3.2.6 Dark Current-Voltage (I-V) Measurement

Current-voltage characteristics of the solar cells provide an investigation of the PV parameters under illumination. In some circumstances, analysis of the I-V curve under dark conditions is the best approach to extract the several parameters of the device. Therefore, a better insight can be inferred about the solar cell properties. The reason is that, in the dark environment, most of the current passes through the emitter since there is no illumination. However, if there is illumination, the current is traveling through the emitter and is collected under the front metal contacts [47].

Dark I-V curves enable us to extract some unknown parameters of the solar cells. These are described in Chapter 2.5. In this thesis, R_{sh} and R_s will be extracted from the dark I-V curves that will be measured. In ODTÜ-GÜNAM laboratories, it is strived to minimize these effects on the cells produced.

CHAPTER 4

EXPERIMENTAL RESULTS

In the first part of the thesis, the influence of the rear metal fraction on solar cell characteristics was studied. In addition, the influence of rear local contact design on PV parameters and BSF formation was also studied. The statistical evaluation of the BSF formation correlated with the cell results.

In the second part of the thesis, the Griddler Pro simulation tool was utilized to determine the front side metal design and fraction. With this tool, an optimal metallization screen was designed. Then, the screen printing parameters were studied with the produced screen. Fast-firing recipe optimizations were achieved and the necessary characterizations were reported on PERC solar cells fabricated in ODTÜ-GÜNAM laboratories.

4.1 Optimization and Characterization of Rear Metal Contacts

4.1.1 The Effects of Rear Metal Fraction on Passivation Quality

The optimum metal fraction for the rear of the PERC solar cell involves a series of studies to determine the point at which rear surface passivation quality is reduced. Four different metal fractions (2.1%, 2.87%, 3.24%, and 4.30%) are formed on the rear side of the PERC. The first three are scribed in the form of the dashed lines, while the last one is scribed as a line pattern. It is observed in Figure 4.1 that the 3.24% metal fraction provides the highest iV_{oc} (after fast-firing) among the all patterns.

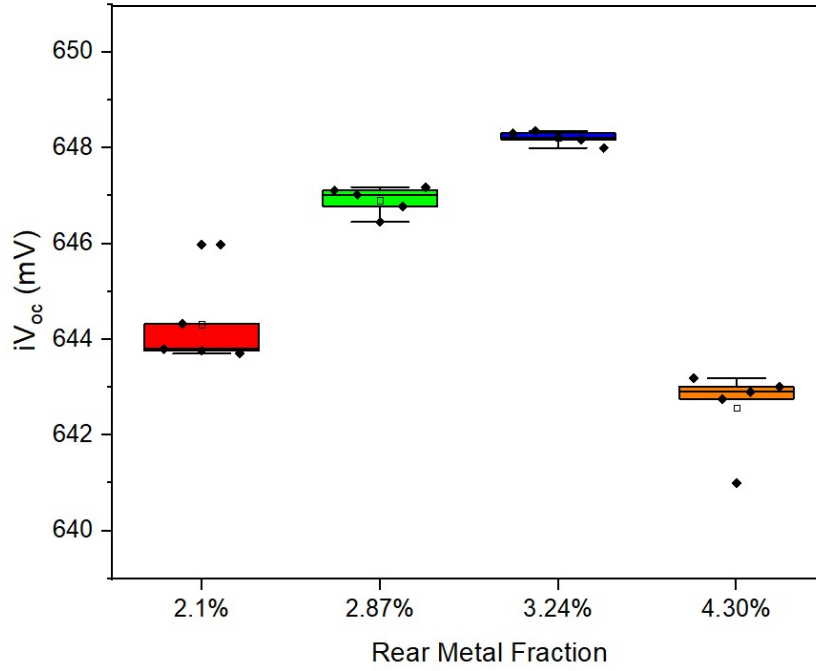


Figure 4.1. iV_{oc} values of the blue wafers lasered by different fractions

The studied patterns have the following specifications as listed in Table 4.1.

Table 4.1. Dimensional specifications of the four patterns

Metal Fraction (%)	Type of Pattern	Contact Width (μm)	Contact Length (mm)	Contact Pitch (μm)
2.1	Dash-1:1	65	0.6	1500
2.87	Dash-2:1	65	1.2	1500
3.24	Dash-3:1	65	1.8	1500
4.30	Line	65	150	1500

The decrease in the iV_{oc} values is started after the 3.24% metal fraction on the rear side of the wafers. The reason is correlated with the deterioration of the rear surface passivation quality.

The all samples for the iV_{oc} measurement have the same contact pitch; 1500 μm . However, an optimization of the contact pitch is required for controlling the BSF formation inside the LCOs.

4.1.2 The Effects of the LCO Pitch on Solar Cell Performance

As suggested in [42], the rear LCO pitch was changed from 900 μm to 1200 μm by an increment of 100 μm on a dashed 1:1 pattern alongside with reference pattern of the line which has a 1500 μm contact pitch. Since the highest iV_{oc} was attained on a 3.24% metal fraction, there is a need for shortening the length of one dashed line while decreasing the contact pitch. Therefore, choosing the 1:1 pattern is an ideal way of reaching the required metal fraction.

K K. Wijekoon et al. have optimized the contact pitch as 900 μm ; therefore, the experiments were started with the same [3]. After the ablation, implied open-circuit voltage (iV_{oc}) values were measured with the quasi-steady state photoconductance (QSSPC) method by the Sinton tool. These results were correlated with photoluminescence (PL) images. Then, Al paste was screen printed on top of the rear surface, and the samples were fired by a conveyor belt furnace. Cell performances were obtained by current-voltage (I-V) measurements with a class AAA solar simulator under the standard test conditions.

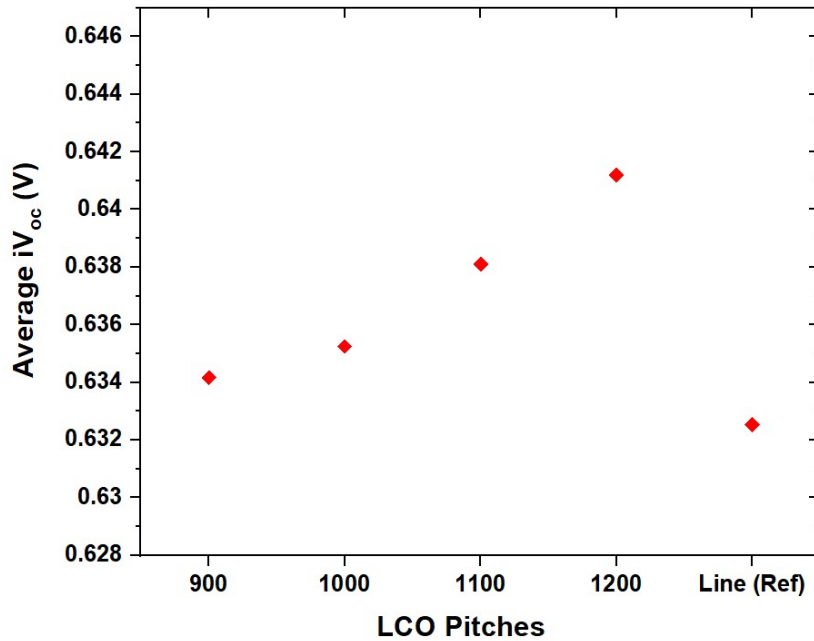


Figure 4.2. Average iV_{oc} chart of the blue wafers lasered with different contact pitches

For each LCO pattern, an identical 10 wafers were included and their average iV_{oc} values were compared. The PL images of selected ones from each LCO parameter were also obtained. As the contact pitch increases from 900 μm to 1200 μm , average iV_{oc} values increase gradually. The highest average iV_{oc} value was obtained by dash pattern with 1200 μm pitch. 8 mV increase on average was obtained with this dashed line pattern compared to the reference line patterned cells. The following Figures 4.3.1-2-3-4-5 denote the PL images of the studied patterns. PL images include a PL intensity chart of all processed patterns below each figure.

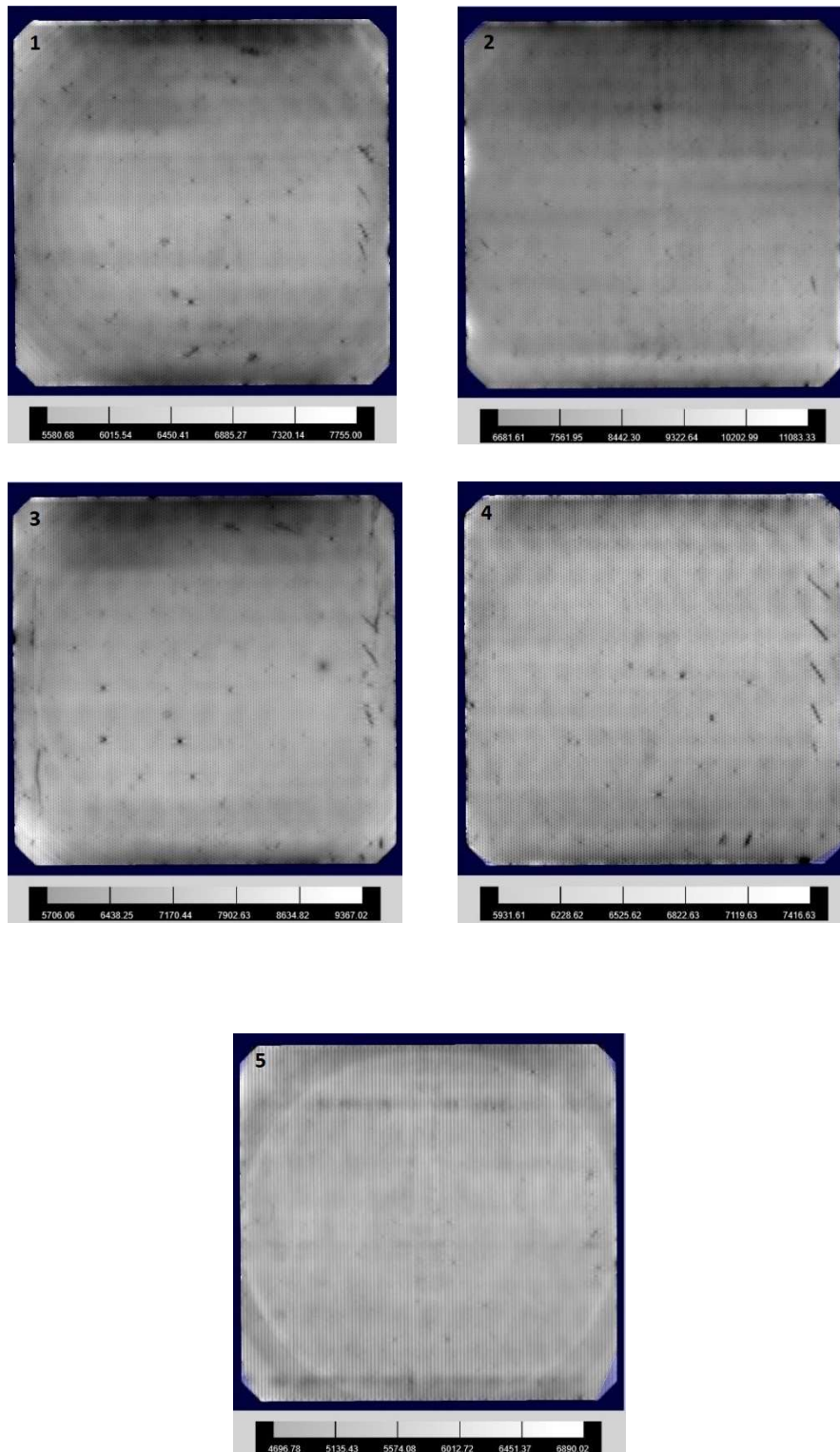


Figure 4.3. PL images for dashed patterns with 900 μm, 1000 μm, 1100 μm, and 1200 μm contact pitches and the line pattern, respectively

Since the Sinton QSSPC method measures the iV_{oc} on a localized region of the full wafer, the PL imaging does a mapping over the surface of the wafer and provides more reliable information. Although the highest iV_{oc} was obtained on the dashed pattern with 1200 μm contact pitch, the PL intensity images show that 1000 μm contact pitch provides a higher PL intensity than 900 μm , 1100 μm , and 1200 μm contact pitches. These predictions are confirmed by I-V measurement results. The average of each photovoltaic parameter can be seen in Table 4.2 and Figure 4.4.

Table 4.2. Average photovoltaic parameters for each LCO pattern

Pattern	V_{oc} (mV)	FF (%)	J_{sc} (mA/cm^2)	Efficiency (%)
Dash-900	659.94	81.18	38.81	20.82
Dash-1000	662.73	81.36	38.85	20.95
Dash-1100	660.44	81.38	38.86	20.88
Dash-1200	658.67	81.17	38.95	20.83
Reference (Line)	656.72	81.01	38.74	20.61

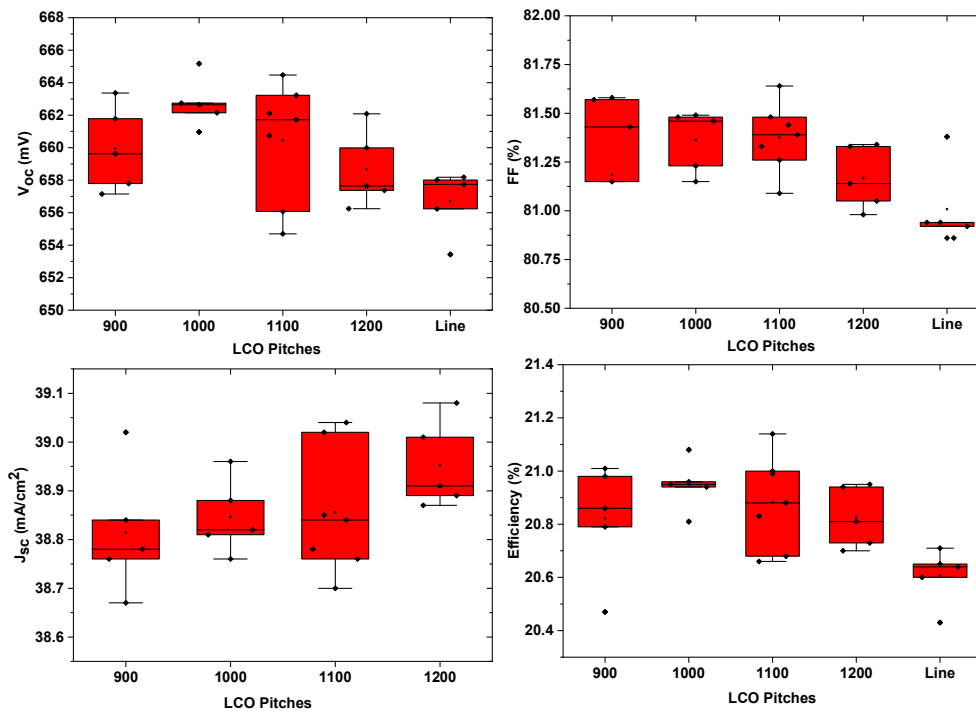


Figure 4.4. Cell conversion efficiencies of all dashed lines with the reference LCO pattern (line pattern)

Table 4.2 and Fig. 4.4 confirm the results of the PL images which are presented in Figures 4.3. Average open-circuit voltage (V_{oc}) results have shown that dash patterns give better results with respect to the line patterned cells. In Table 4.2 and Fig. 4.4, it is evident that the dashed line pattern with 1000 μm contact pitch surpassed the line pattern and it is found to be beneficial for the rear surface LCO because of low V_{oc} losses.

4.1.3 The Effects of LCO Pitch on Contact Characteristics

The laser contact opening pitch should be minimum to form a back surface field (BSF) through the local contacts. This is due to the distribution of the silicon content inside the screen-printed aluminum paste. Therefore, the distance between two successive contacts should be small for good BSF formation since there should be enough silicon inside the Al paste between them [42]. On the other hand, with the decreasing LCO pitch, the back surface passivation quality deteriorates with the damage caused by the laser. The optimized LCO pattern provides a minimum metal fraction and a higher percentage of BSF or local-BSF formation. Table 4.3 shows the number of voids, BSF, and local-BSF for each contact pitch. For this analysis, the rear local contacts from each fabricated solar cell were investigated under the SEM. In the fifth column, the percentages of BSF/local-BSF formed contacts were tabulated. In addition, Figure 4.5 represents the well-formed BSF image through the LCO.

The dash-1000 pattern provides the highest percentage of the BSF/local-BSF formed contacts among the all patterns.

Table 4.3. *Statistical contact characteristics of the investigated contacts*

Pattern (1:1)	Total Number of Investigated Contacts	Number of Void Formed Contacts	Number of BSF or local-BSF Formed Contacts	Percentage of BSF/ Local-BSF Formed Contacts (%)
Dash-900	437	350	87	20
Dash-1000	333	140	193	58
Dash-1100	368	228	140	38
Dash-1200	438	280	158	36
Reference (Line)	332	263	69	21

When these results are evaluated from the perspective of metal fractions, an increase of metal fraction up to one point heals the cell characteristics. This critical point has been determined in this study as 3.19% (Dash-1000) which the best cell characteristics were obtained.

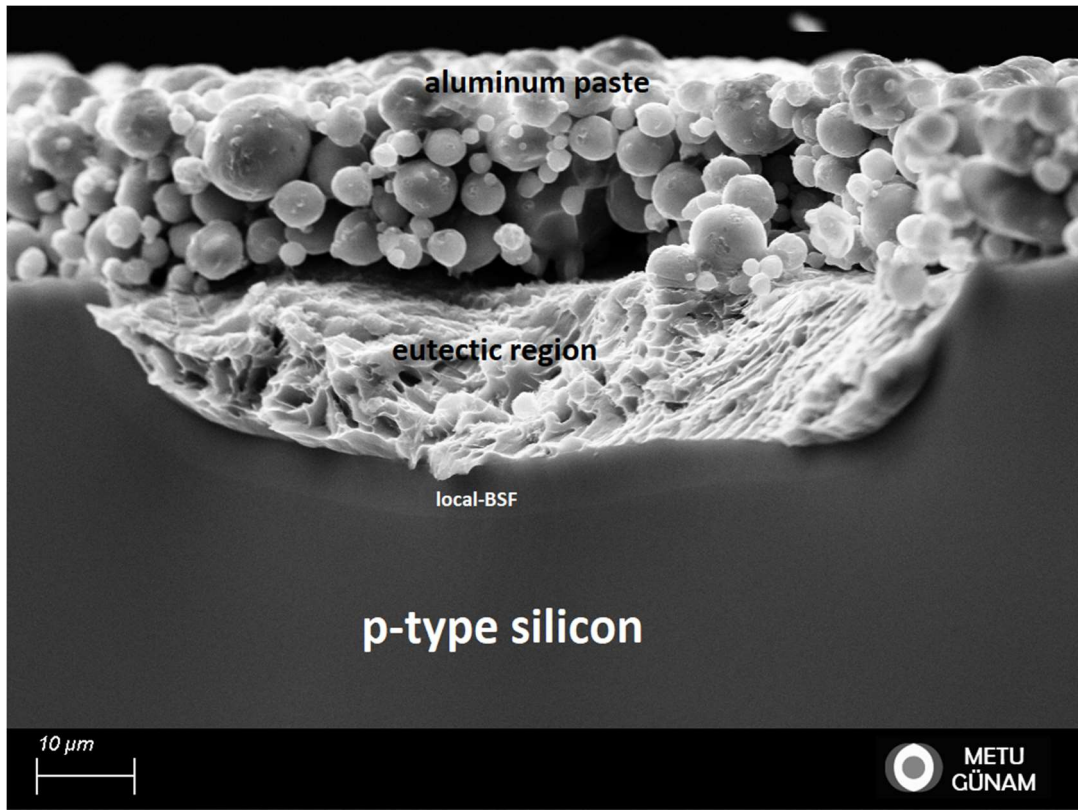


Figure 4.5. Well-formed BSF under the LCO with Dash-1000 pattern

From the results of Table 4.2 and Table 4.3, it can be concluded that higher V_{oc} values are directly related to the high percentage of the BSF/local-BSF formed contacts. Also, LCO pitch is a determinant factor in the BSF formation.

4.2 Optimization and Characterization of the Front Metal Contacts

4.2.1 Simulation of the Front Metal Grid Design via GriddlerPro

The PERC solar cell structure was simulated with the information transferred from our lab to the simulation tool GriddlerPro. The necessary information was supplied from the characterization tools such as ECV, 4PP, TLM, reflection measurement, etc.

Table 4.4 shows the PV parameters that are set for the simulations. (* denotes that the input is supplied by our data)

Table 4.4. *Simulation parameters*

Parameter	Value
Finger sheet resistance	2 mOhm/sq
Busbar sheet resistance	3 mOhm/sq
Finger contact resistance	0.5 mOhm.cm ²
Layer sheet resistance*	94.7 Ohm/sq
J ₀₁ (passivated area)*	112 fA/cm ²
J ₀₁ (metallized area)	572 fA/cm ²
Front illumination	1 Suns
Wafer thickness*	180 μm
Base resistivity*	1.1.Ohm-cm
Rear passivation SRV*	35 cm/s
Rear LCO width*	65 μm
Rear LCO pitch*	1000 μm

The PERC solar cell structure is simulated to determine the optimum front metallization fraction. The number of front fingers, finger widths, metalized area, and the PV parameters that will be targeted are extracted from the results of the simulations.

Starting from 4% metal fraction, varying fractions are simulated up to 10%. Figure 4.6 shows the corresponding solar cell performances for each metal fraction. It is determined that the above 7% metal fraction distorts the passivation quality of the solar cell and the decreasing trend is seen in the simulated cells. A 5.5% metal fraction, on the other hand, gives the best solar cell performance.

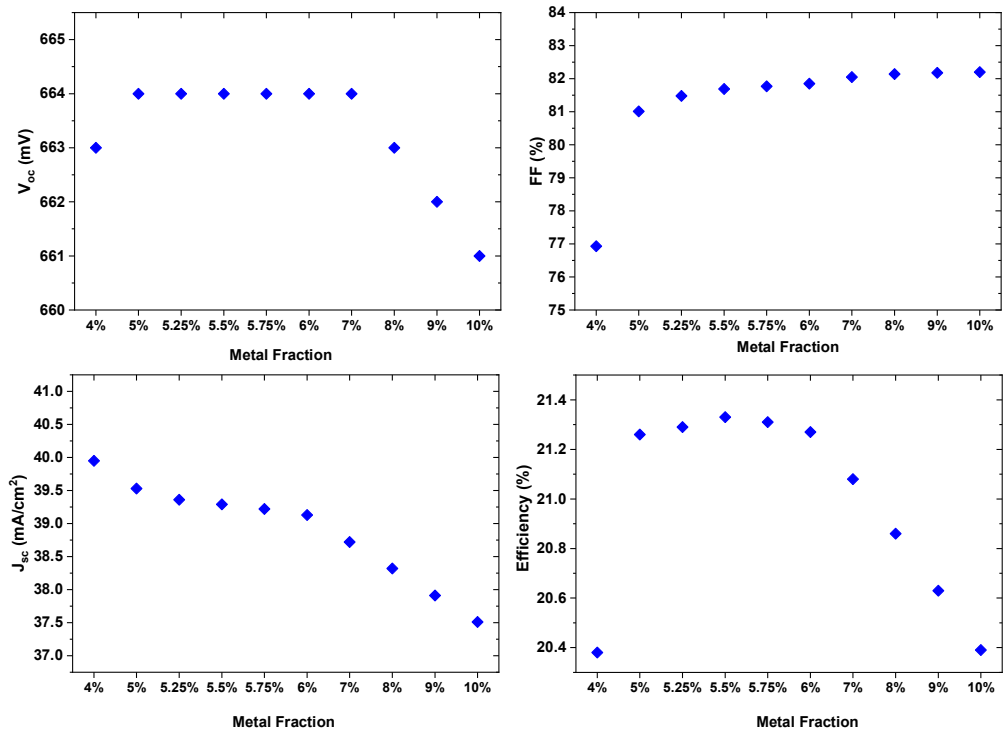


Figure 4.6. Simulated results of the PERC solar cells with varying front metal fractions

To determine the optimum width of fingers by using the results in Figure 4.6, varying finger widths from 25 μm to 40 μm are simulated on PERC solar cells with a metal fraction of around 5.5%. The results of the simulations are tabulated in Figure 4.7.

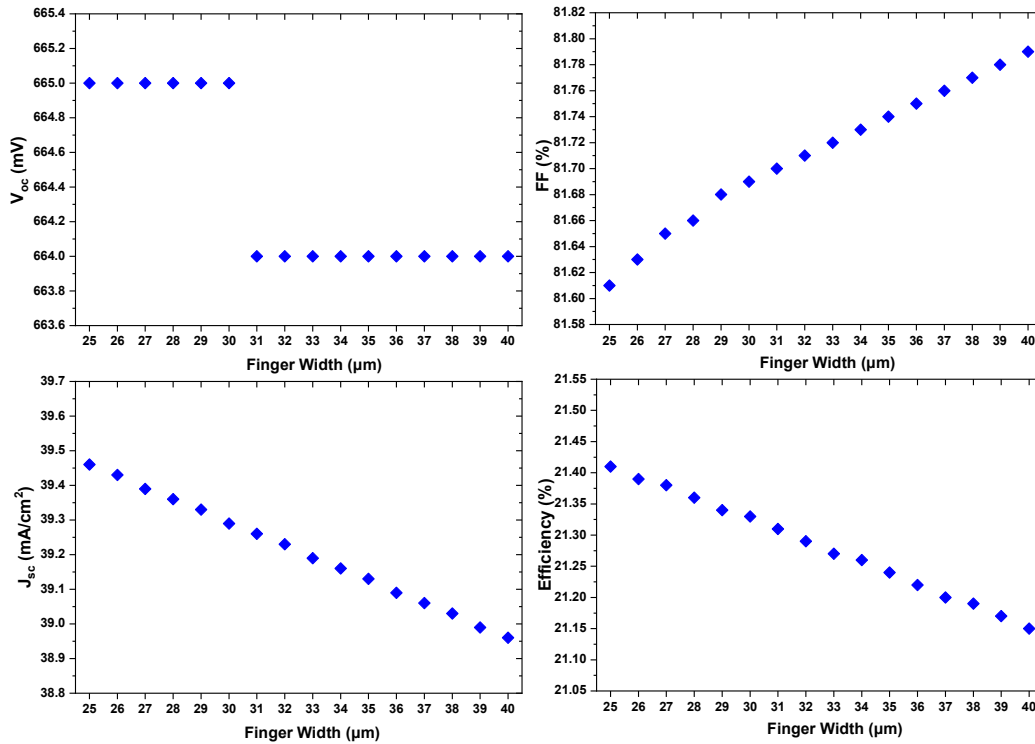


Figure 4.7. Simulated results of the PERC solar cells with varying finger widths around 5.5% metal fraction

Due to the current-carrying capability and less shadowing effect, narrower fingers are more desirable for the PERC solar cell to obtain the highest efficiency. Therefore, the results of Figure 4.7 are a guide for choosing the optimum finger width. PERC solar cells with 25 μm finger width provide the best solar cell conversion efficiency. However, it is the poorest one in terms of FF. Low FF is evidence of high series resistance in a solar cell. Also, a 1 mV decrease is observed on the V_{oc} 's after a 30 μm finger width case. Therefore, the fingers in the range of 25 μm to 30 μm widths are the best candidates. The 30 μm width was chosen since it is the less resistive one between 25 μm to 30 μm . In addition, one should consider the specs of the solar cell pastes because too narrow fingers will create disconnections which result in a loss in the FF and J_{sc} .

The final results of the simulation give PERC solar cell design as tabulated in Table 4.5.

Table 4.5. *Final screen specs from simulated data*

Parameter	Value
Metallization area	244.3 cm ²
Number of fingers	129
Number of busbars	5
Finger width	30 μm
Busbar width	1000 μm
Edge gap	500 μm

4.2.2 Process Integration of the Simulated Results

A metallization screen that has the properties tabulated in Table 4.5 is produced by a well-known company Koenen GmbH in Germany. According to the suggestions of the company and the specs of the Ag pastes that we have (two different brands), the physical properties and the limits of the produced metallization screen are listed in Table 4.6.

Table 4.6. *Specs of the metallization screen*

Parameter	Value
Mesh number	430
Wire diameter	13
Finger width	≤ 28 μm
EOM thickness	≤ 15 μm

With the produced screen, printing parameters are studied and aspect ratio analysis is achieved by using SEM. Since the highest printed fingers and narrow widths are

aimed, the snap-off parameter should be optimized. Firstly, the printing speed and the squeegee pressure constant were kept constant. With these fixed values, the snap-off distance is varied from 1000 μm to 2000 μm by an increment of 100 μm .

Table 4.7. *Printing parameters for the snap-off test*

Parameter	Value
Squeegee speed	200 mm/s
Squeegee pressure	80 N
Snap-off distance	1000 μm – 2000 μm

For this analysis, two types of Ag paste from two different brands, Heraeus Photovoltaics, and Pharos Materials, were used. A Standard fast-firing recipe is applied for the production of the samples. For each sample, metal contacts are investigated under the SEM and Figure 4.8 shows the aspect ratio values for each sample.

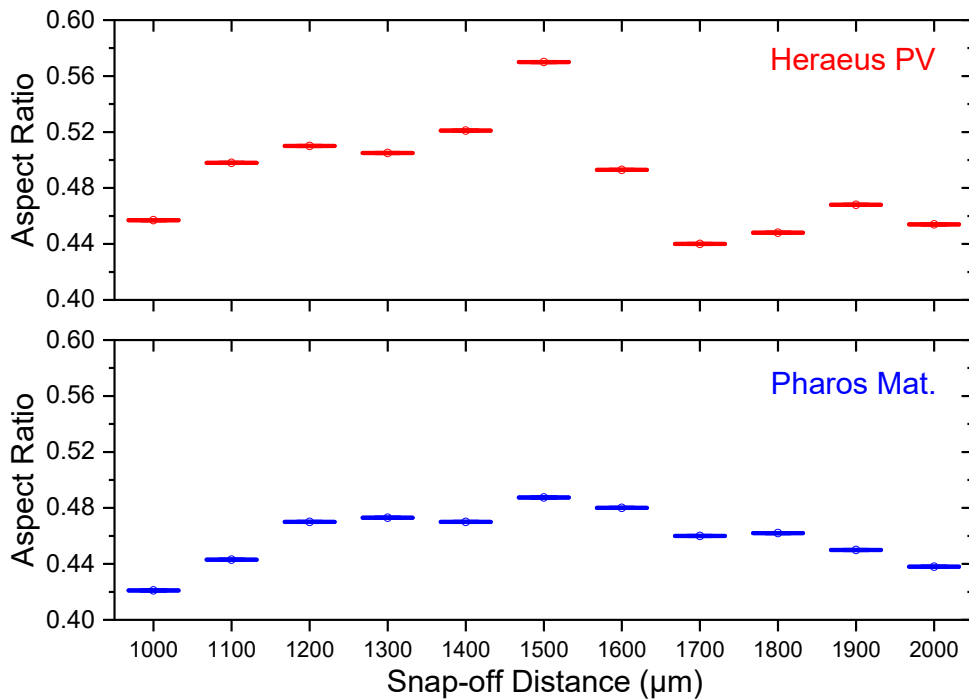


Figure 4.8. Snap-off distance vs. aspect ratio for Heraeus PV (top) and Pharos Materials (bottom) Ag paste

From the results of Figure 4.8, it is noted that the 1500 μm snap-off distance provides the best aspect ratio for both paste brands. In addition, a 0.57 aspect ratio was achieved with the Heraeus PV Ag paste (SOL9661B). In the Heraeus Ag paste datasheet, the highest aspect ratio is shown as 0.4424 as seen in Figure 4.9. Also, in [48], they achieved a 0.47 aspect ratio with double printing.

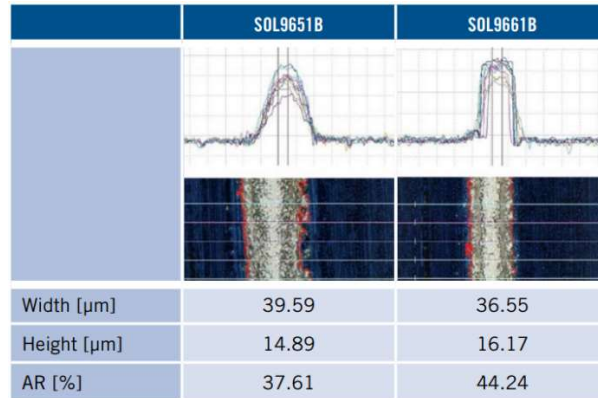


Figure 4.9. Aspect ratios of the Heraeus PV paste [49]

Since a very promising result about aspect ratio was obtained by setting the snap-off distance to 1500 μm , that value is used for the processes. An outstanding difference is not observed when the squeegee speed and pressure were changed, they were kept constant at 200 mm/s and 80 N, respectively.

4.2.3 The Effects of Fast-Firing Profiles on Contact Characteristics and PV Parameters

With these two paste brands, LCO and metallization processes were done on the blue wafers to produce PERC solar cells. The fast-firing profile optimization is done starting from the three fast-firing profiles indicated in Chapter 3.1.4. The initial firing profile (Recipe-1) of the ODTÜ-GÜNAM provides the results as shown in Table 4.8 for each specified region that was defined in Chapter 3.1.4. It is compared with the other two profiles from best know companies.

Table 4.8. Analysis of the regions on three different fast-firing recipes

Profile	1 st region ramp rate	Plateau Region	3 rd region ramp rate	Time intervals above 600 °C	Cooling rate
Recipe-1	34.6 °C/s	450 °C – 4.5s	26.8 °C/s	11 s	36 °C/s
Fraunhofer	36.6 °C/s	500 °C – 7.3s	106.6 °C/s	5.3 s	58.6 °C/s
Heraeus	34.6 °C/s	475 °C – 6.5s	73.5 °C/s	5.4 s	101 °C/s

To make optimization on each zone in correlation with the PV parameters, the following temperatures are set and analyzed with the same technique as Table 4.8.

Table 4.9. Fast-firing set temperatures

Profile	Zone-1 Temp. (°C)	Zone-2 Temp. (°C)	Zone-3 Temp. (°C)	Zone-4 Temp. (°C)	Zone-5 Temp. (°C)	Zone-6 Temp. (°C)	Belt Speed (cm/min)
1	350	450	550	650	750	785	380
2	350	450	550	650	650	785	380
3	350	450	550	550	750	785	380
4	350	450	550	550	750	885	380
5	350	450	550	550	550	885	380
6	350	550	550	550	550	885	380
7	350	500	500	500	500	885	380
8	350	500	500	500	500	885	360
9	350	500	500	500	500	855	410
10	350	500	500	500	500	825	410

The 9 different fast-firing profiles were measured. Then, each region named 1 to 5 was analyzed. The followings are our aims and the proofs for these temperatures.

- 1- Standard fast-firing profile.
- 2- Zone-5 is decreased by 100 °C.
Aim: To sharpen the 3rd region ramp rate and decrease the time above 600 °C.
- 3- Zone-4 is decreased by 100 °C.
Aim: To sharpen the 3rd region ramp rate and decrease the time above 600 °C.
- 4- Zone-6 is increased by 100 °C.
Aim: To sharpen the 3rd region ramp rate and heal the contact characteristics.
Proof: A few metalized blue wafers are fired and fill factors were too low.
- 5- Zone-5 is decreased by 100 °C.
Aim: To sharpen the 3rd region ramp rate and decrease the time above 600 °C.
Proof: A few metalized blue wafers are fired and there was significantly low shunt resistance on cells.
- 6- Zone-2 is increased by 100 °C.
Aim: To increase the temperature of the plateau region as well as to be flattened the profile. Plateau region prepares the printed aluminum for melting. ($T_{\text{melt}} = 660,3 \text{ °C}$)
- 7- Zones 2-3-4-5 are decreased by 100 °C.
Aim: Minimize the V_{oc} losses due to high temperature during firing.
Proof: A few metalized blue wafers are fired and low V_{oc} values (less than 5 mV) are obtained compared to the previous studies. 65 °C actual decrease around the plateau region healed the V_{oc} .
- 8- Belt speed is decreased by 20 mm/s.
Aim: Minimize the series resistance resulting in low FFs and eliminate the high contact resistance problem.
Proof: A few metalized blue wafers are fired and low FFs obtained. After belt speed optimization, we reached below 5 mOhm.cm² about R_c .

9- Zone-6 temperature is decreased by 30 °C and belt speed is increased by 50 mm/s.

Aim: Minimize the shunt resistance via minimum reduction of peak temperature (Zone-6) to protect FF.

Proof: A few metalized blue wafers are fired and low shunt resistances are obtained. The temperature at which FF is protected is determined on Zone-6 and this healing is supported by the increase of the belt speed.

10- Zone-6 temperature is decreased by 30 °C

Aim: To protect the passivation quality of the cells without causing a reduction in front metal contact quality.

Proof: A few blue wafers are metalized and the highest cell V_{oc} is obtained. Also, contact resistivity around 1.5 mOhm.cm² was attained.

Table 4.10. *Analysis of the fast-firing final profile*

Profile	1 st region ramp rate	Plateau Region	3 rd region ramp rate	Time intervals above 600 °C	Cooling rate
First Profile	34.6 °C/s	450 °C – 4.5s	26.8 °C/s	11 s	36 °C/s
Final Profile	29.4 °C/s	475 °C – 7s	30.7 °C/s	5 s	38.3 °C/s
Fraunhofer	36.6 °C/s	500 °C – 7.3s	106.6 °C/s	5.3 s	58.6 °C/s
Heraeus	34.6 °C/s	475 °C – 6.5s	73.5 °C/s	5.4 s	101 °C/s

Figure 4.10 and Figure 4.11 shows the measured temperatures of the initial and final profiles as a function of time.

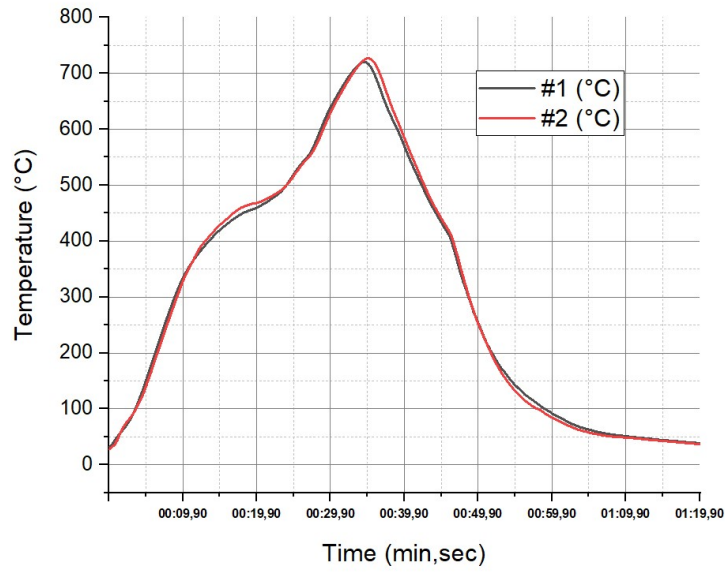


Figure 4.10. Initial profile of ODTÜ-GÜNAM

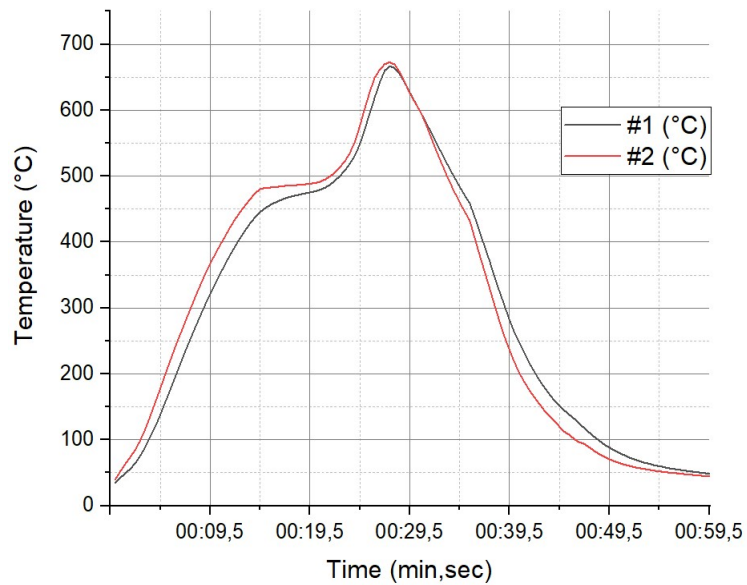


Figure 4.11. Final profile of ODTÜ-GÜNAM

The final recipe has a peak temperature of 825° as well as a belt speed of 410 cm/min. After the fast-firing recipe optimization, the PERC solar cells from blue wafers with Heraeus PV and Pharos Materials Ag pastes were produced. The results are shown in Figure 4.12.

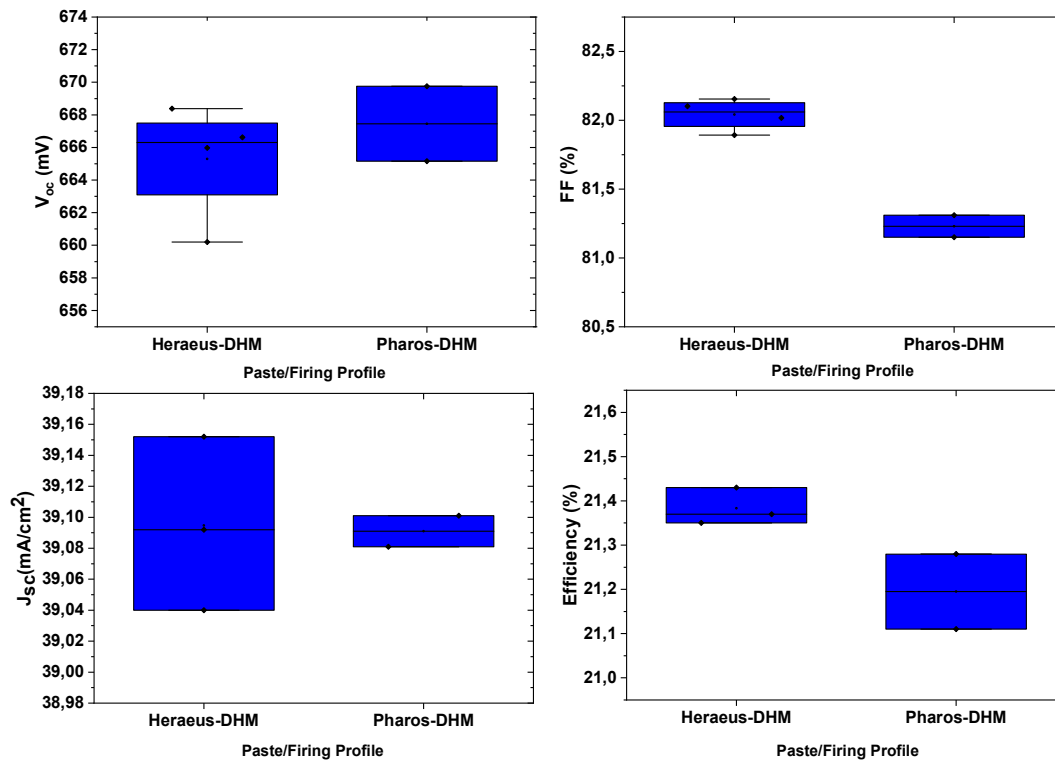


Figure 4.12. Comparison of the cell results printed with Heraeus and Pharos pastes

As shown in Figure 4.12, Heraeus PV Ag paste provided an almost 1% average FF increase compared to the Pharos Materials Ag paste. The reason for this remarkable difference is caused by the high series resistance measured on the solar cell printed with Ag paste of Pharos Materials. Dark I-V measurement is conducted on the produced solar cells and the R_s values are reported by the dark I-V curves.

Table 4.11. R_s values of the PERC solar cells produced with two different Ag pastes

Paste	R_s (Ohm.cm ²)
Heraeus PV Ag Paste	1.21
Pharos Mat. Ag Paste	10.51

The solar cell printed with two paste groups was cut into the 7 slices and the contact resistivities of the metal fingers on each slice were measured. The difference between FF and R_s is also correlated with the R_c results in Figures 4.13 and 4.14.

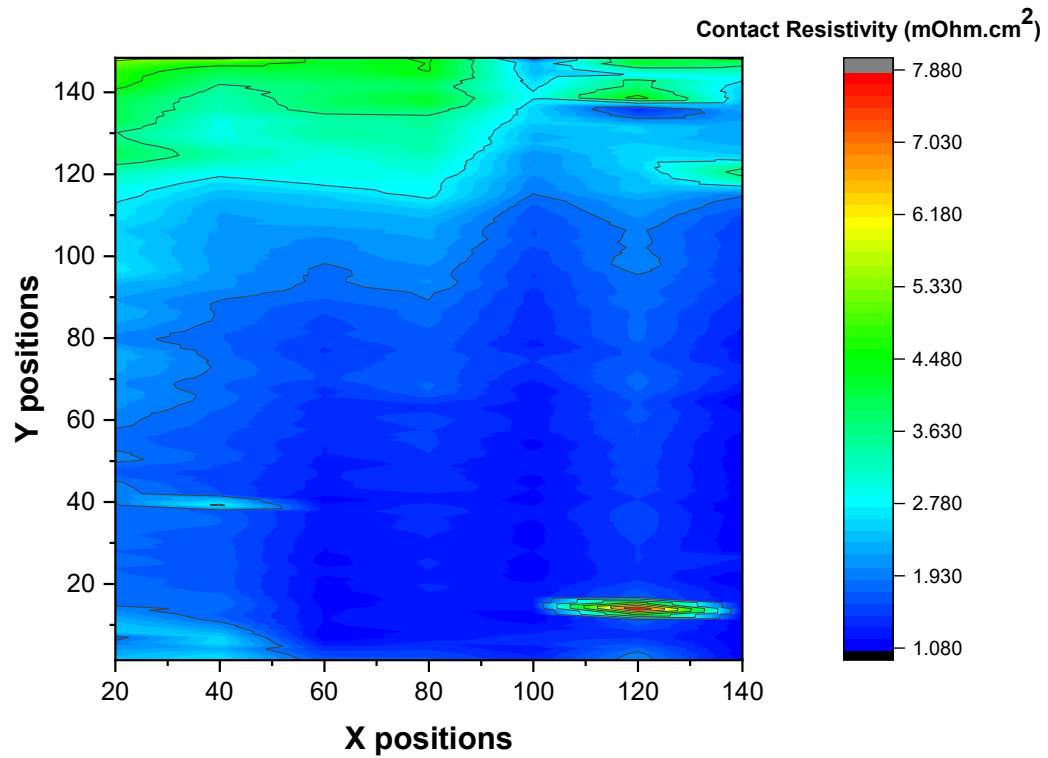


Figure 4.13. Contact resistivities of the metal fingers printed with Heraeus PV Ag paste

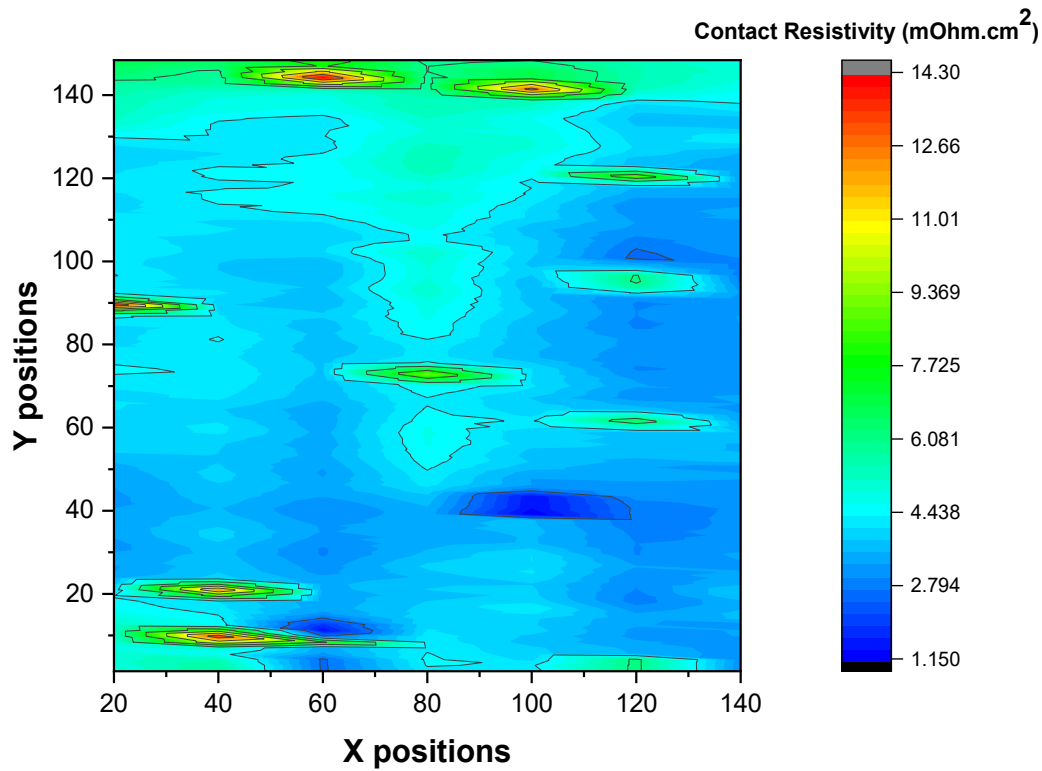


Figure 4.14. Contact resistivities of the metal fingers printed with Pharos Mat. Ag paste

The average of the contact resistivities between metal fingers and the emitter is reported as 1.92 mOhm.cm² for Heraeus PV Ag paste and 4.0 mOhm.cm² for Pharos Materials Ag paste.

In addition to these results, SEM images of the printed metals are investigated to see the sintering quality. Figure 4.15 and Figure 4.16 shows the SEM images of the metal fingers printed with Heraeus PV and Pharos Materials Ag pastes, respectively.

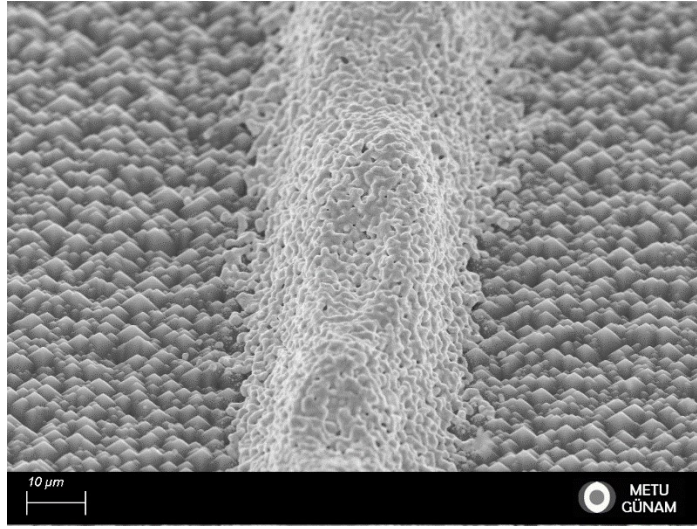


Figure 4.15. SEM image of the metal finger printed with Heraeus PV Ag paste

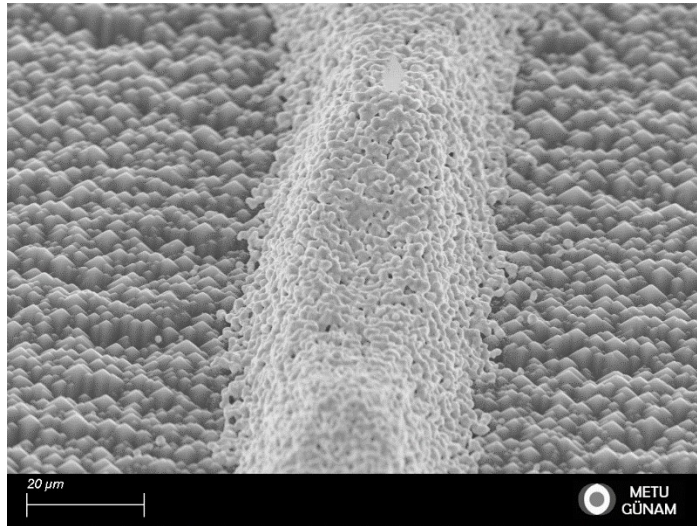


Figure 4.16. SEM image of the metal finger printed with Pharos Materials Ag paste

At the same fast-firing recipe, almost identical sintering qualities can be observed on the SEM images.

After these optimizations on the blue wafers, our know-how is integrated into the PERC solar cells fabricated in ODTÜ-GÜNAM. Since the wafer parameters are almost identical compared to the blue wafers, ODTÜ-GÜNAM cells are metallized with the same procedure described for the blue wafers. Heraeus PV Ag paste is used for the metallization of the samples. The results show that the cell performances were

improved with the optimizations that were done on the front and rear surface metallizations. Table 4.12 shows the best cell result of the PERC solar cell fabricated in the ODTÜ-GÜNAM PV line.

Table 4.12. *PV parameters of the best solar cell fabricated in ODTÜ-GÜNAM*

Sample Name	V_{oc} (mV)	FF (%)	J_{sc} (mA/cm ²)	Efficiency (%)
Group 4-DHM	660.4	81.61	38.99	21.02

A 21.02% conversion efficiency is achieved with the improvements in the front and rear metallization as well as the passivation layers.

The calculated series resistance from the dark I-V curve for the PERC solar cells fabricated in ODTÜ-GÜNAM is tabulated in Table 4.13.

Table 4.13. *R_s of the solar cell fabricated in ODTÜ-GÜNAM*

Sample Name	R_s (Ohm.cm ²)
Group 4-DHM	2.79

The contact resistivities of the produced PERC solar cell are described in Figure 4.18. An average of 1.65 mOhm.cm² contact resistivity is obtained from the produced solar cell.

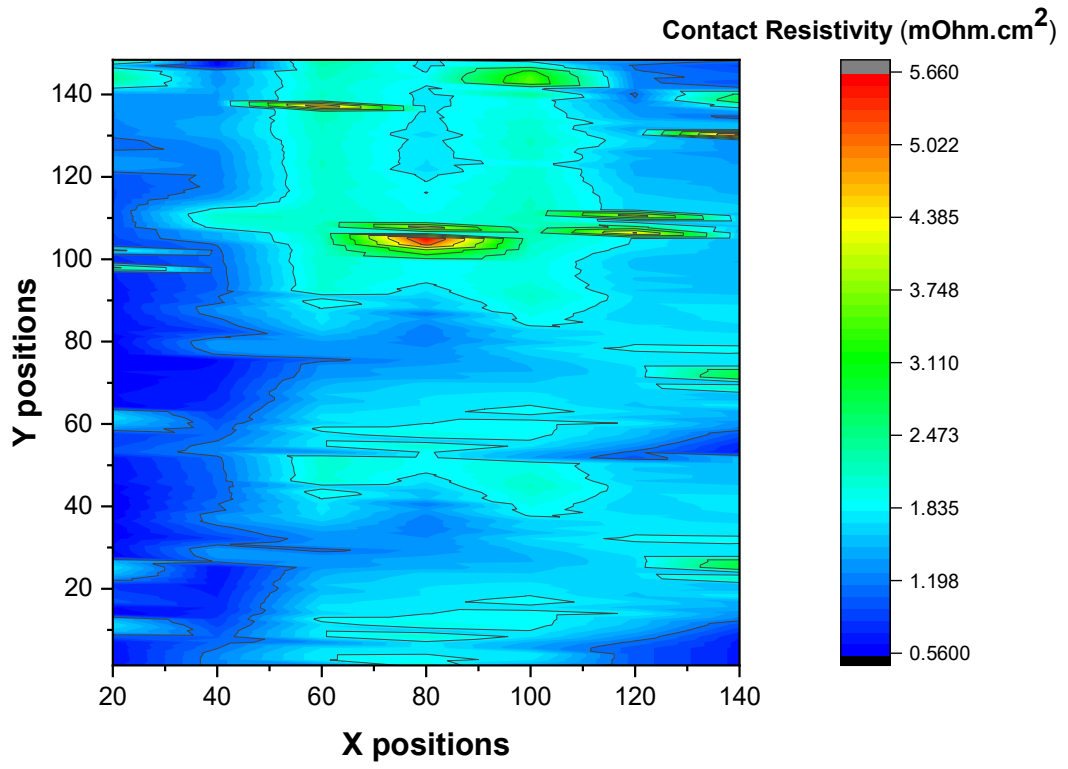


Figure 4.17. Contact resistivity mapping of the ODTÜ-GÜNAM cells

CHAPTER 5

CONCLUSIONS

In this study, it is investigated that the rear local contact openings for PERC solar cell have a profound impact on the protection of the rear side passivation quality. The optimization of the rear metal fraction determines the optimum point for the percentage of rear side ablation. For this optimization, the dashed line pattern is created while considering the minimum ablation at which the highest iV_{oc} and PL intensity were obtained. An increase of metal fraction up to one point heals the cell characteristics. This critical point has been determined in this study as 3.19% which the best cell performances were attained. The laser contact opening pitch should be minimum to form a back surface field through the local contacts. This is due to the distribution of the silicon content inside the screen-printed aluminum paste [50]. Therefore, the distance between two successive contacts should be small for good BSF formation since there should be enough silicon inside the Al paste between them [50]. On the other hand, with the decreasing LCO pitch, the back surface passivation quality deteriorates with the damage caused by the laser. The optimized LCO pattern provides a minimum metal fraction and a higher percentage of BSF/local-BSF formation.

The BSF layer protects the rear side of the solar cell from the recombinations. Extra-heavy doping at the rear creates a field that keeps the minority carriers (electrons) from the highly recombining rear surface. The reduction in recombination increases the electron concentration in the base, therefore, the solar cell voltage is increased. In this study, the solar cell V_{oc} is increased by 6 mV with the optimizations on the rear side LCO pattern.

In the second part of the thesis study, front side metal contacts are investigated and the optimum metal fraction is determined by using the Griddler Pro simulation tool.

The simulation results show that 5.5% front metal coverage will benefit the cell characteristics more. The simulated results are integrated into the process, and remarkably similar cell characteristics are obtained. Two different brands of Ag pastes are processed and compared. For each type of paste, snap-off distance (wafer to screen distance) is optimized and aspect ratio analysis is performed via SEM. While industrial companies can print the front metal fingers with an aspect ratio of around 0.44, we achieved a 0.57 aspect ratio.

The last optimizations are done on the fast-firing recipe in ODTÜ-GÜNAM laboratories. The recipe formation is started with the analysis of the examples from industrial companies & laboratories. A method is devised to analyze the fast-firing profiles and this analysis shows the temperature variations, rates, and times that the cell is subjected. The fast-firing profile is divided into the five regions and these regions specify the ramp rates during heating (1st and 3rd ramp rates in Figure 3.8), the time that passed during the plateau region (around 450 °C), the time that passed above 600 °C and the cooling rate after the wafer is exposed to the peak temperature. Each region has a different effect on the cell's characteristics. It can be concluded that the first region initializes the cell for the fast-firing process since organic binders and solvents are removed from the paste during this heating. The plateau region has a major effect on the liquifying of the Al paste since Al is melted at 660 °C. The time that the cell is exposed above 600 °C heals the contact characteristics and the R_c is minimized with a proper optimization while protecting the passivation quality. For this analysis, two Ag paste brands are processed and it is found that the final fast-firing profile matches well with the Heraeus PV Ag paste. Although Pharos Materials Ag paste provides good results in terms of cell parameters, the final fast-firing profile should be developed more to increase the performance of PERC solar cells printed with Pharos Materials Ag paste.

As a result of the optimizations conducted on the PERC solar cell front and rear metallization, 21.02% conversion efficiency is achieved on the PERC solar cells fabricated in ODTÜ-GÜNAM.

REFERENCES

- [1] Energy and climate change. European Environment Agency. (2021, May 11). Retrieved May 16, 2022, from <https://www.eea.europa.eu/signals/signals-2017/articles/energy-and-climate-change>
- [2] Global Energy Review 2021 - .NET framework. (n.d.). Retrieved May 16, 2022, from <https://iea.blob.core.windows.net/assets/d0031107-401d-4a2f-a48b-9eed19457335/GlobalEnergyReview2021.pdf>
- [3] www.ren21.net. (n.d.). Retrieved May 16, 2022, from https://www.ren21.net/wp-content/uploads/2019/05/GSR2021_Full_Report.pdf
- [4] Ritchie, H., Roser, M., & Rosado, P. (2020, November 28). Renewable energy. Our World in Data. Retrieved May 16, 2022, from <https://ourworldindata.org/renewable-energy>
- [5] Lafond, F., Bailey, A. G., Bakker, J. D., Rebois, D., Zadourian, R., McSharry, P., & Farmer, J. D. (2017). How well do experience curves predict technological progress? A method for making distributional forecasts.
- [6] Nature research. (n.d.). Retrieved May 16, 2022, from <https://www.nature.com/articles/am201082.pdf>
- [7] Crystalline silicon photovoltaics research. Energy.gov. (n.d.). Retrieved May 16, 2022, from <https://www.energy.gov/eere/solar/crystalline-silicon-photovoltaics-research>
- [8] *Global Solar Power to cross 200 GW annual installation threshold in 2022*. Balkan Green Energy News. (2021, July 22). Retrieved June 13, 2022, from <https://balkangreenenergynews.com/global-solar-power-to-cross-200-gw-annual-installation-threshold-in-2022/>
- [9] Solar Manufacturing Cost Analysis. NREL.gov. (n.d.). Retrieved May 16, 2022, from <https://www.nrel.gov/solar/market-research-analysis/solar-manufacturing-cost.html>
- [10] Rühle, S. (2016). Tabulated values of the Shockley–Queisser limit for single junction solar cells. *Solar Energy*, 130, 139–147. <https://doi.org/10.1016/j.solener.2016.02.015>
- [11] 4.5. Types of PV technology and recent innovations | EME 812: Utility Solar Power and Concentration. (n.d.). Retrieved May 16, 2022, from <https://www.e-education.psu.edu/eme812/node/608>
- [12] R. Akhter and . A. Hoque, "Analysis of a PWM Boost Inverter for Solar Home Application," in *World Academy Of Science, Engineering And Technology*, 2006.

- [13] F. A. Lindholm, Fossum, J. G., and Burgess, E. L., “Application of the superposition principle to solar-cell analysis”, *IEEE Transactions on Electron Devices*, vol. 26, pp. 165–171, 1979.
- [14] Morales-Aragonés, J.I.; Alonso-García, M.d.C.; Gallardo-Saavedra, S.; Alonso-Gómez, V.; Balenzategui, J.L.; Redondo-Plaza, A.; Hernández-Callejo, L. Online Distributed Measurement of Dark I–V Curves in Photovoltaic Plants. *Appl. Sci.* 2021, 11, 1924, doi:10.3390/app11041924
- [15] A. Goetzberger, J. Knobloch and B. Voss, *Crystalline Silicon Solar Cells*, Wiley & Sons Ltd., 1998.
- [16] H. Seidel et al, “Anisotropic Etching of Crystalline Silicon in Alkaline Solutions: I. Orientation Dependence and Behavior of Passivation Layers“, 1990 *J. Electrochem. Soc.* 137 3612
- [17] Baker-Finch, SC & McIntosh, KR 2013, ‘Reflection distributions of textured monocrystalline silicon: implications for silicon solar cells’, *Progress in Photovoltaics: Research and Applications*, vol. 21, no. 5, pp. 960–971.
- [18] Pang-Kai Liu, Yu-Lun Cheng, Likarn Wang, "Crystalline Silicon PERC Solar Cell with Ozonized AlOx Passivation Layer on the Rear Side", *International Journal of Photoenergy*, vol. 2020, Article ID 6686797, 6 pages, 2020. <https://doi.org/10.1155/2020/6686797>
- [19] Kapila Wijekoon, Fei Yan, Yi Zheng, Dapeng Wang, Hemant Mungekar, Lin Zhang, Hari Ponnekanti, "Optimization of Rear Local Contacts on High Efficiency PERC Solar Cells Structures", *International Journal of Photoenergy*, vol. 2013, Article ID 368403, 8 pages, 2013. <https://doi.org/10.1155/2013/368403>
- [20] Kuo, C., Kuan, T., Liu, C., Huang, C., Wu, L., & Yu, C. (n.d.). Impact of Laser Opening Ratio for Mass Production High Efficiency Mono-Crystalline Silicon Solar Cells. *Di*, 1392–1394.
- [21] E. Urrejola, K. Peter, H. Plagwitz, and G. Schubert, “Distribution of Silicon in the Aluminum Matrix for Rear Passivated Solar Cells” *Energy Procedia*, vol. 8, pp.331, 2011.
- [22] Urrejola E, Peter K, Plagwitz H, Schubert G. Silicon diffusion in aluminum for rear passivated solar cells. *Appl. Phys. Lett.* 2011;98:153508.
- [23] A. Paul, Ph.D. thesis, Technische Universiteit Eindhoven, 2004.
- [24] Laser pulses power energy equations - Thorlabs. (n.d.). Retrieved May 16, 2022, from https://www.thorlabs.com/images/tabimages/Laser_Pulses_Power_Energy_Equations.pdf

- [25] Mohammed, M. K., Umer, U., Abdulhameed, O., & Alkhalefah, H. (2019). Effects of laser fluence and pulse overlap on machining of microchannels in alumina ceramics using an nd:YAG laser. *Applied Sciences*, 9(19), 3962. <https://doi.org/10.3390/app9193962>
- [26] A. Lorenz, M. Linse, H. Frintrup, M. Jeitler, A. Mette, M. Lehner, R. Greutmann, H. Brocker, M. König, D. Erath, and F. Clement, 35th European Photovoltaic Solar Energy Conference and Exhibition, 819 (2018).
- [27] Retrieved from “Screen-Printed Front Junction n-Type Silicon Solar Cells” by Y. Tao, 2016, Printed Electronics - Current Trends and Application
- [28] S. Thibert, J. Jourdan, B. Bechevet, J. Faissat, S. Mialon, D. Chaussy, N. Reverdy-Bruas, and D. Beneventi, “Combining design of experiments and power loss computations to study the screen printing process,” in 2013 IEEE 39th Photovoltaic Specialists Conference (PVSC): 16 - 21 June 2013, Tampa, Florida (IEEE, Piscataway, NJ, 2013), p. 2280.
- [29] AIP Conference Proceedings 2156, 020006 (2019); <https://doi.org/10.1063/1.5125871>
- [30] E.J. Lee et al. / *Solar Energy Materials & Solar Cells* 74 (2002) 65–70
- [31] Tepner, S., Ney, L., Singler, M., Preu, R., Pospischil, M., & Clement, F. (2021). A model for screen utility to predict the future of printed solar cell metallization. *Scientific Reports*, 11(1). <https://doi.org/10.1038/s41598-021-83275-0>
- [32] Hahne, P., (2001). *Innovative Drucktechnologien Siebdruck- Tampondruck Auflage*, Germany
- [33] Uzum, A., Ashikaga, T., Noguchi, T., Kanda, H., Fukui, H., Harada, T., & Ito, S. (2020). Development of aluminum paste with/without boron content for crystalline silicon solar cells. *Materials Research Express*, 7(3), 035502. <https://doi.org/10.1088/2053-1591/ab77ee>
- [34] PVEducation. (n.d.). Retrieved May 16, 2022, from <https://www.pveducation.org/>
- [35] Retrieved from “Screen-Printed Front Junction n-Type Silicon Solar Cells” by Y. Tao, 2016, Printed Electronics - Current Trends and Application
- [36] M. Müller, G. Fischer, B. Bitnar, et al., "22.61% efficient fully screen printed PERC solar cell," *Energy Procedia*, vol. 124, pp. 131-137, 2017.

- [37] J. Weber, S. Lohmüller, E. Lohmüller et al., "Simulations on laser-phosphorous-doped selective emitters," in 7 th World Conference on Photovoltaic Energy Conversion, to be published, 2018.
- [38] A. Wolf, A. Kimmerle, S. Werner, et al., "Status and perspective of emitter formation by POCl₃- diffusion," in 31st European Photovoltaic Solar Energy Conference and Exhibition, 2015, pp. 414- 419.
- [39] S. Werner, E. Lohmüller, S. Maier, et al., "Challenges for lowly-doped phosphorus emitters in silicon solar cells with screen-printed silver contacts," *Energy Procedia*, vol. 124, pp. 936-946, 2017.
- [40] ITRPV, "International technology roadmap for photovoltaic (ITRPV) - 2017 Results - Ninth edition, March 2018," available online: <http://www.itrpv.net/Reports/Downloads/>, 2018.
- [41] Optimization of PERC fabrication based on loss analysis in an industrially relevant environment: First results from GÜNAM photovoltaic line (GPVL), *Renewable Energy*, Volume 146, 2020, Pages 1676-1681, ISSN 0960-1481, <https://doi.org/10.1016/j.renene.2019.07.149>.
- [42] Chiu, J.-S., Zhao, Y.-M., Zhang, S., & Wu, D.-S. (2020). The role of laser ablated backside contact pattern in efficiency improvement of mono crystalline silicon perc solar cells. *Solar Energy*, 196, 462–467. <https://doi.org/10.1016/j.solener.2019.12.044>
- [43] *Impact of firing temperature profiles on local BSF formation in perc ...* (n.d.). Retrieved June 13, 2022, from http://www.metallizationworkshop.info/fileadmin/metallizationworkshop/favicon/6.1_Mack_MetWS.pdf
- [44] Manual, U. (2018). User Manual 1 - 1. *Strain*, 2–7.
- [45] Nanakoudis, A. (2022, February 18). *What is sem? scanning electron microscopy explained*. Accelerating Microscopy. Retrieved May 16, 2022, from <https://www.thermofisher.com/blog/microscopy/what-is-sem-scanning-electron-microscopy-explained/>
- [46] Trupke, T., Mitchell, B., Weber, J. W., McMillan, W., Bardos, R. A., & Kroeze, R. (2012). Photoluminescence imaging for Photovoltaic Applications. *Energy Procedia*, 15, 135–146. <https://doi.org/10.1016/j.egypro.2012.02.016>
- [47] Zhao, J., A., Dai, Green, & Wenham. (n.d.). Dark IV measurements. PVEducation. Retrieved May 16, 2022, from

<https://www.pveducation.org/pvcdrom/characterisation/dark-iv-measurements>

- [48] Galiazzo, M., Furin, V., Tonini, D., Cellere, G., & Baccini, A. (2010). DOUBLE PRINTING OF FRONT CONTACT AG IN c-Si SOLAR CELLS. 25th European Photovoltaic Solar Energy Conference and Exhibition / 5th World Conference on Photovoltaic Energy Conversion, 6-10 September 2010, Valencia, Spain, November, 2010–2013.

- [49] *SOL9661B series - heraeus*. (n.d.). Retrieved June 29, 2022, from https://www.heraeus.com/media/media/hpt/doc_hpt/metallization_pastes_downloads/Spotlight_SOL9661B_EN_V07.pdf

- [50] E. Urrejola, K. Peter, H. Plagwitz, G. Schubert, Understanding and avoiding the formation of voids for rear passivated silicon solar cells, Presentation at the 3rd Metallization Workshop, Charleroi, Belgium, 201141